

Depinning, front motion, and phase slips

Y.-P. Ma^{a)} and E. Knobloch

Department of Physics, University of California, Berkeley, California 94720, USA

(Received 27 March 2012; accepted 12 June 2012; published online 5 July 2012)

Pinning and depinning of fronts bounding spatially localized structures in the forced complex Ginzburg-Landau equation describing the 1:1 resonance is studied in one spatial dimension, focusing on regimes in which the structure grows via roll insertion instead of roll nucleation at either edge. The motion of the fronts is nonlocal but can be analyzed quantitatively near the depinning transition. © 2012 American Institute of Physics. [<http://dx.doi.org/10.1063/1.4731268>]

When a spatially periodic wave train invades a stable, spatially homogeneous state, the periodic structure has to be grown behind the moving front separating them. Two processes are frequently involved, wavelength stretching and the insertion of new structure. In general, these processes interact, for example, the stretching can trigger phase slips corresponding to cell-splitting, whose effect is then redistributed across the structure. Thus, the front speed that results is determined by the dynamics not only at the location of the front but also behind it. These processes are illustrated and analyzed using a simple partial differential equation in one spatial dimension.

I. INTRODUCTION

In recent years, there has been growing interest in spatially localized structures (LS) in forced dissipative systems described by partial differential equations (PDEs) in one or more spatial dimensions. Such states include spot-like structures found in reaction-diffusion systems,¹³ as well as states referred to as convectons that arise in various types of convection.^{4,6,7} Related structures are present in subcritical shear flows.²⁹ The LS in these systems are typically time-independent although they can undergo both spontaneous and forced translation as explored recently in models based on the Swift-Hohenberg equation.^{8,16} In other systems, such as Faraday waves, the LS oscillate in time, either periodically or with a more complex time-dependence, forming structures referred to as oscillons.^{20,25} This is also the case for oscillons in granular media³² and in optics.¹ Other examples of LS include localized traveling waves^{3,18} and three-dimensional states called “worms” arising in electroconvection.^{15,26} In many of these systems, the use of envelope equations removes the (fast) time-dependence and maps such time-dependent structures onto equilibria of an envelope equation.

The structures mentioned above are all examples of “dissipative solitons” in which energy loss through dissipation is balanced by energy input through spatially homogeneous forcing and are located in regions of parameter space in which a spatially homogeneous state A coexists with a second state B, either a homogeneous state or a spatially

periodic state. In the former case, the LS consists of an inclusion of a homogeneous state B in a background of state A (Type-I LS); in the latter, the LS consists of an inclusion of a periodic state B in a background of state A (Type-II LS). Extended LS of either type can be viewed as a bound state of a pair of fronts connecting A to B and back again. Extended Type-I LS are of codimension one and so exist only at isolated parameter values. In contrast, extended Type-II LS are of codimension zero and so are found within an interval of parameter values. This fact may be ascribed to the phenomenon of self-pinning, whereby the fronts pin to the spatial oscillations between them.²⁴ Outside of the resulting *pinning region* the fronts depin, allowing either state A or the periodic state B to invade the domain.

These phenomena are simplest to understand physically in systems with gradient structure for which a free energy \mathcal{E} may be derived. This is the case, for example, for the Swift-Hohenberg equation.^{9,10} The presence of a free energy allows one to define the Maxwell point, the parameter value at which states A and B possess equal energies. The pinning mechanism implies that a stationary bound state of a pair of fronts between A and B persists throughout a parameter interval Δr straddling the Maxwell point r_M . Depinning occurs once $|r - r_M|$ is sufficiently large that the free energy difference $|\mathcal{E}_A - \mathcal{E}_B|$ exceeds the pinning energy. In the simplest case, the fronts move via the nucleation of new cells at the location of the front; existing cells remaining stationary, implying that the motion of the front is akin to that of a forest fire with the advancing front indicating the location of the conversion of unburnt material (state A) into burnt material (state B). This type of motion is quite well understood largely because the motion of the front is related to instability that is localized in the region of the front.^{9,10}

Similar behavior is found in many systems with non-gradient dynamics. However, such systems exhibit other types of depinning dynamics as well. For example, the structure can grow via the splitting of the central cell and the subsequent outward push of the preexisting cells on either side.²² In other situations, there may be two locations where new cells are inserted via phase slips so that only a part of the existing structure is pushed outward.²² These two types of behavior have one thing in common: as the fronts on either side move apart the cells within the structure are stretched, and it is this increase in wavelength that triggers

^{a)}Present address: Department of Geophysical Sciences, University of Chicago, Chicago, Illinois 60637, USA.

Eckhaus instability and results in the generation of a phase slip. This phase slip leads in turn to a readjustment in the wavelength of the structure, and if this wavelength falls in the Eckhaus-stable regime, no further phase slips take place until the continuing front motion pushes the wavelength back into the Eckhaus-unstable regime. This paper is devoted to a detailed understanding of the nexus between front motion and the phase slips it triggers. In particular, we show that the phase slips occur in specific regions of the wavetrain and examine how the location and time of the phase slips depend on the width of the wavetrain and the distance from the parameter value for pinning.

II. THE FORCED COMPLEX GINZBURG-LANDAU EQUATION

We focus on the dynamics of the 1:1 forced complex Ginzburg-Landau equation for a complex scalar field $A(x, t)$,^{12,22} hereafter FCGLE,

$$\frac{\partial A}{\partial t} = (\mu + i\nu)A - (1 + i\beta)|A|^2A + (1 + i\alpha)\nabla^2A + \gamma. \quad (2.1)$$

As shown in Ref. 22, this equation has nongradient dynamics and exhibits the type of depinning dynamics summarized in Sec. I. In the following, we shall find it useful to rewrite Eq. (2.1) in terms of U and V , the real and imaginary parts of $A \equiv U + iV$,

$$\begin{bmatrix} U_t \\ V_t \end{bmatrix} = \left(\begin{bmatrix} \mu & -\nu \\ \nu & \mu \end{bmatrix} + \begin{bmatrix} 1 & -\alpha \\ \alpha & 1 \end{bmatrix} \partial_{xx} - (U^2 + V^2) \begin{bmatrix} 1 & -\beta \\ \beta & 1 \end{bmatrix} \right) \times \begin{bmatrix} U \\ V \end{bmatrix} + \begin{bmatrix} \gamma \\ 0 \end{bmatrix}, \quad (2.2)$$

and use both representations interchangeably.

Equation (2.1) possesses two types of time-independent solutions, homogeneous states for which $A_{xx} = 0$ and periodic states for which $A_{xx} \neq 0$. In appropriate parameter regimes, the former form an S-shaped branch in the $(\gamma, |A|)$ diagram, and we denote the three coexisting equilibria by $A^+/A^0/A^-$ (upper/middle/lower). The stability of the equilibria is described by temporal eigenvalues σ satisfying the quadratic equation

$$\begin{aligned} \sigma^2 - 2\sigma(\mu - k^2 - 2R_2) + (1 + \alpha^2)k^4 \\ + 2[2(1 + \alpha\beta)R_2 - (\mu + \alpha\nu)]k^2 + \mu^2 + \nu^2 \\ - 4(\mu + \beta\nu)R_2 + 3(1 + \beta^2)R_2^2 = 0, \end{aligned} \quad (2.3)$$

where $R_2 \equiv |A|^2$ and k is the wavenumber of the perturbation. Analysis of this equation identifies two types of instability. The first has critical wavenumber $k=0$ and corresponds to either a saddle-node ($\sigma = 0$) or a Hopf bifurcation ($\sigma = \pm i\omega$). The second has critical wavenumber $k \neq 0$ and is known as the Turing instability. It is also important to consider the *spatial* stability of the homogeneous states. The spatial eigenvalues λ satisfy a quadratic equation in λ^2

$$\begin{aligned} (1 + \alpha^2)\lambda^4 - 2[2(1 + \alpha\beta)R_2 - (\mu + \alpha\nu)]\lambda^2 + \mu^2 \\ + \nu^2 - 4(\mu + \beta\nu)R_2 + 3(1 + \beta^2)R_2^2 = 0. \end{aligned} \quad (2.4)$$

In the absence of self-excitation ($\mu < 0$), hyperbolic equilibria (the two roots λ^2 are either both complex or both positive real) are temporally stable, while elliptic equilibria (at least one root λ^2 is negative real) are Turing-unstable.²³ The periodic states are time-independent solutions of Eq. (2.1) which are periodic in x and respect reversibility, i.e., they are invariant under $x \rightarrow -x$ relative to a suitable origin. The spatial stability of such states is likewise related to temporal stability. A hyperbolic periodic state (real Floquet multipliers) is temporally stable, while an elliptic state (Floquet multipliers on the unit circle) is not. An unstable wavetrain of the latter type rapidly readjusts its wavelength into a stable configuration through the generation of phase slip(s). This phenomenon is known as the Eckhaus instability.¹⁷

Throughout this paper, we fix the parameters at $\alpha = -1.5$, $\beta = 6$, and $\mu = -1$ (the damped case), but allow ν and γ to vary. In Sec. III, we focus on the process of depinning near the boundaries of the pinning region containing Type-I LS, while Sec. IV tackles the more challenging case of Type-II LS. In both cases, we seek to understand quantitatively how the speed c of the depinned front depends on the distance from the boundary of the pinning region and the details of the nucleation process leading to front advance. We conclude with some open questions in Sec. V.

III. DEPINNING OF TYPE-I LS

In this section, we study Type-I LS consisting of an interval of the upper homogeneous state A^+ embedded in a background of the lower homogeneous state A^- . We fix $\nu = 5$ and study Type-I LS as a function of the remaining parameter γ . Figure 1 shows that steady Type-I LS lie on a collapsed snaking branch that collapses to a single value of γ as one follows it from its origin at the right saddle-node (SN) of the homogeneous states towards larger amplitude as measured by the norm

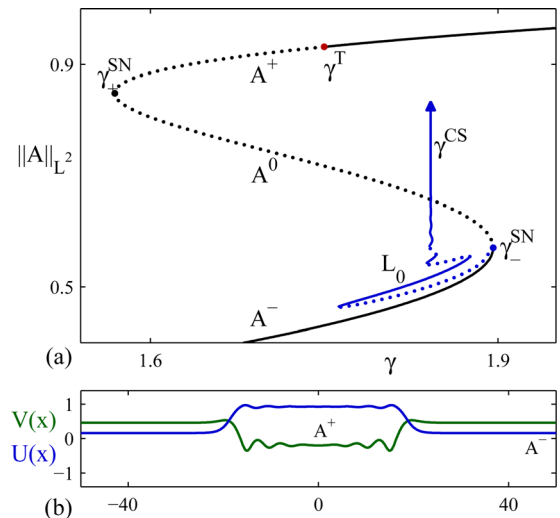


FIG. 1. (a) Bifurcation diagram at $\alpha = -1.5$, $\beta = 6$, $\mu = -1$ and $\nu = 5$, where the branch L_0 of steady LS undergoes collapsed snaking to γ^{CS} . Stable (unstable) segments are shown in solid (dotted) lines on both the L_0 branch and the S-shaped branch of homogeneous equilibria. For clarity, only the first three unstable segments on L_0 are indicated. (b) A sample solution high up the L_0 branch.

$$\|A\|_{L^2} \equiv \sqrt{\frac{1}{\ell} \int_{-\ell/2}^{\ell/2} \{|A(x)|^2 + |A_x(x)|^2\} dx}, \quad (3.1)$$

where ℓ is the large but finite period of the periodic domain used in the computation. The figure shows that the collapse point is $\gamma^{CS} = 1.8419$, while the right saddle-node is at $\gamma_-^{SN} = 1.8958$ and the left saddle-node is at $\gamma_+^{SN} = 1.5694$; the Turing instability occurs at $\gamma^T = 1.7501$ and generates periodic states with wavenumber $k_T = 1.2868$. In the following, we define $d\gamma = \gamma - \gamma^{CS}$ and study the solution behavior in the bistable region $\gamma_+^{SN} < \gamma < \gamma_-^{SN}$.

A. Type-I time evolution

Type-I depinning only occurs for LS of finite length since infinitely long LS are only present at $\gamma = \gamma^{CS}$. At this value of γ , there is a large multiplicity of stable steady LS of finite length. We take one of these (e.g., Fig. 1(b)) as an initial condition and solve Eq. (2.1) at $\gamma \neq \gamma^{CS}$ using the ETD2 time-stepping scheme.¹⁴ As shown in Figs. 2(a) and 2(b), the plateau of A^+ expands for $\gamma > \gamma^{CS}$ and shrinks for $\gamma < \gamma^{CS}$. In the former case, the domain is eventually filled with A^+ . In the latter case, the final state is either a stable pulse with background A^- (if such exists) or A^- everywhere (otherwise).

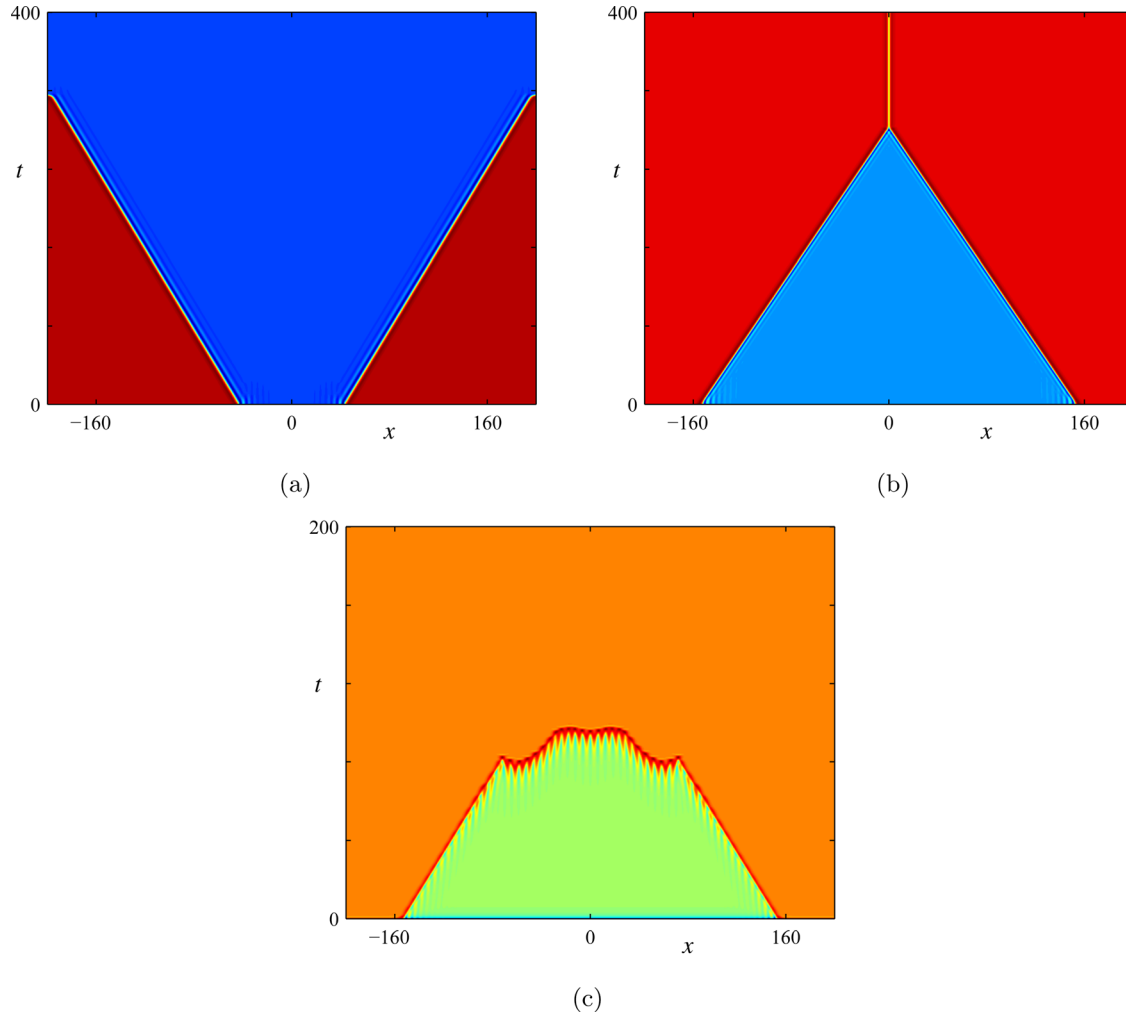


FIG. 2. Space-time plots of $V(x, t)$ showing Type-I LS depinning at (a) $d\gamma = 0.04$; (b) $d\gamma = -0.04$; (c) $d\gamma = -0.24$.

The region $\gamma < \gamma^T$ is particularly interesting. In this case, A^+ is Turing-unstable and tends to evolve into a periodic state. If this happens before the depinning ends, the subsequent evolution will be altered. Indeed, as shown in Fig. 2(c), the periodic state may evolve more rapidly into A^- thereby shortening the overall depinning process.

The speed c of the *left* front is plotted as a function of γ in Fig. 3 (open circles); c depends smoothly on $d\gamma$ with $c \sim d\gamma$ as $d\gamma \rightarrow 0$. Thus $c > 0$ corresponds to a shrinking LS, while $c < 0$ corresponds to an expanding LS.

B. Analysis of Type-I depinning

The above results can be understood in terms of front motion. Each front of a broad LS is well approximated by a heteroclinic connection between A^- and A^+ , i.e., by a solution of the spatial dynamics problem on the real line. A moving front can likewise be approximated by the corresponding solution on the real line. It follows that a left front moving with speed c solves the equation

$$(1+i\alpha)A_{\xi\xi} + cA_\xi + \gamma + (\mu + i\nu)A - (1+i\beta)|A|^2A = 0, \quad (3.2)$$

where $\xi \equiv x - ct$, subject to the boundary conditions $A(\pm\infty) = A^\pm$, and similarly for a right front. Such moving

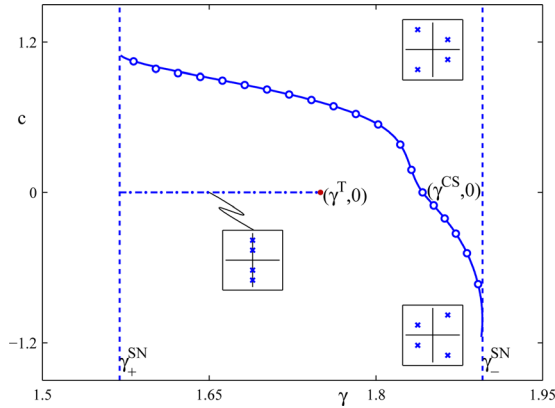


FIG. 3. Plot of the front speed c as a function of γ at $\nu = 5$. Open circles: DNS of Eq. (2.1). Solid line: continuation of heteroclinic orbits in Eq. (3.2). Vertical dashed lines: SN bifurcations (left/right: $\gamma_{+/-}^{SN}$). Horizontal dotted-dashed line: RB bifurcations on A^+ . The insets show the eigenvalue configuration of A^\pm in Eq. (3.2) for different signs of c .

fronts or equivalently heteroclinic orbits \mathbb{H} between A^\pm can then be superposed back to back to approximate the expanding or shrinking states shown in Fig. 2.

The states A^\pm represent equilibria of the 4D ordinary differential equation (ODE) (Eq. (3.2)). If both have two stable and two unstable (spatial) eigenvalues, \mathbb{H} is of codimension-1. We may follow \mathbb{H} numerically with AUTO by imposing Neumann boundary conditions on a domain of length $\ell \gg 1$ and an integral constraint that factors out the translational invariance with respect to ξ . The result, shown in the (γ, c) -plane in Fig. 3 (solid line), is a smooth curve that passes through the data points from direct numerical simulation (DNS).

When $c=0$, the state A^+ is elliptic when $\gamma_+^{SN} < \gamma < \gamma^T$ and hyperbolic for $\gamma > \gamma^T$. Within Eq. (3.2), viewed as a dynamical system in ξ with c as a parameter, A^+ exhibits different types of bifurcations depending on the value of γ . Specifically, when $\gamma_+^{SN} < \gamma < \gamma^T$ and c varies, the spatial eigenvalues move off the imaginary axis, with one complex conjugate pair moving to the left half plane while the other moves into the right half plane. We call this type of bifurcation a “reversibility-breaking” (RB) bifurcation, and note that when $c > 0$, it is the pair with larger imaginary part (i.e., larger wavenumber) that moves into the left half plane, while the opposite is the case when $c < 0$. In contrast, when $\gamma > \gamma^T$ and $c=0$, the spatial eigenvalues form a complex quartet and so remain bounded away from the imaginary axis when c becomes nonzero. The condition for the eigenvalues to leave the imaginary axis in opposite directions rather than in the same direction, i.e., for a dissipation-induced instability,¹⁹ is derived in Appendix A. Similar results apply to A^- but the Turing bifurcation is absent. From the loci of the SN and RB bifurcations indicated in Fig. 3, we observe that the locus of \mathbb{H} stretches between SN^\pm and never intersects the locus of RB. Hence, along the locus of \mathbb{H} neither A^+ nor A^- undergoes a bifurcation and \mathbb{H} exists in the entire bistable region.

As reviewed in Ref. 27, the spectrum of the front between A^\pm , namely, its temporal eigenvalues in the comoving frame, inherits the essential spectrum of A^\pm . The latter is

obtained from Eq. (2.1) by going into the comoving frame $(\xi, \tau) = (x - ct, t)$, writing $A = R(1 + a(\xi, \tau))\exp i\phi$, linearizing in $a(\xi, \tau)$ and looking for solutions of the form $a(\xi, \tau) = a_+ \exp(ik\xi + s\tau) + \bar{a}_- \exp(-ik\xi + \bar{s}\tau)$. The set of s admitted by this dispersion relation, defined as the essential spectrum Σ_{ess} , can be calculated to be $\Sigma_{ess}(c) = \Sigma_{ess}(c=0) + ikc$, where $\Sigma_{ess}(c=0) = \{s : s \leq s_{max} \in \mathbb{R}\}$ with $s_{max} > 0$ due to the Turing instability. Thus, the Turing instability ($0 < s \in \mathbb{R}$) for $c=0$ manifests itself as a convective instability ($\Re(s) > 0, \Im(s) \neq 0$) for $c \neq 0$.

In view of the absence of a pinning region for Type-I LS, there is no front pinning in the limit of very large LS. Consequently, the speed $c(\gamma)$ passes smoothly through $c=0$ as γ passes through γ^{CS} . Appendix B discusses the corresponding situation in variational systems.

IV. DEPINNING OF TYPE-II LS

Type-II LS arise when the state B is periodic in space. Because B is structured, a pinning region opens out in γ containing time-independent localized states. In systems with a free energy even parity localized states in this region lie on a pair of snaking branches with interconnecting branches of asymmetric localized states, comprising the so-called snakes-and-ladders structure of the pinning region.⁹ In this section, we study depinning from a different type of snaking behavior called defect-mediated snaking (DMS). Figure 4 shows an example of a DMS branch computed at $\nu = 7$ and labeled L_0 . In contrast to the $\nu = 5$ case shown in Fig. 1, for $\nu = 7$, the branch lies to the left of γ^T and enters a snaking interval $\gamma_1^{DMS} < \gamma < \gamma_2^{DMS}$. The growth mechanism of stationary LS in this region is shown in Fig. 5. The DMS branch consists of uniform segments and defect segments which extend, respectively, from γ_1^{DMS} to γ_2^{DMS} and from γ_2^{DMS} to γ_1^{DMS} as one follows the branch upwards. A stationary LS on a uniform segment resembles a periodic wave train connected to A^- by a pair of fronts, while a stationary LS on a defect segment resembles the one on the uniform segment

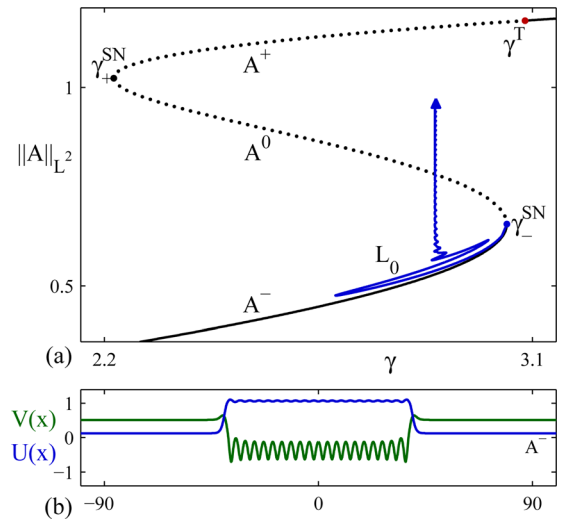


FIG. 4. (a) Bifurcation diagram at $\nu = 7$, where the branch L_0 of steady LS undergoes defect-mediated snaking between $\gamma_1^{DMS} = 2.8949$ and $\gamma_2^{DMS} = 2.8970$. Stability on the branch of equilibria is as in Figure 1, but stability on L_0 is not indicated. (b) A sample solution high up the L_0 branch.

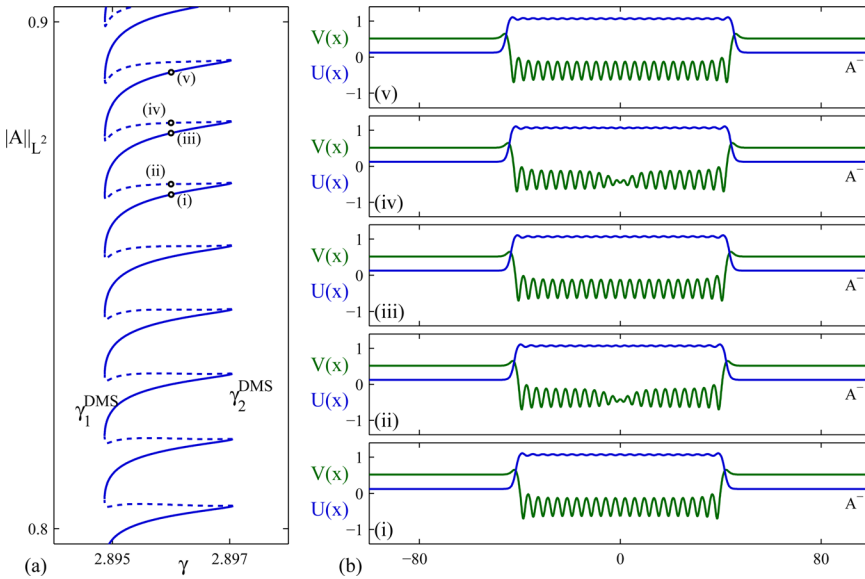


FIG. 5. (a) Detail of the L_0 snaking branch in Figure 4. Temporally stable (unstable) segments are shown as solid (dashed) lines and coincide with uniform (defect) segments. (b) Five sample profiles at $\gamma = 2.896$.

at the same γ , except for the presence of a *defect* in the middle of the wave train. Each time the branch passes through a defect segment, the defect splits and inserts an extra wavelength at the center of the stationary LS. Numerically, we find that the snaking limits are $\gamma_1^{DMS} = 2.8949$ and $\gamma_2^{DMS} = 2.8970$, while the saddle-nodes of the equilibria are located at $\gamma_+^{SN} = 2.2197$ and $\gamma_-^{SN} = 3.0463$ (γ^T lies outside the bistable region). In the following, we define $d\gamma = \gamma - \gamma_1^{DMS}$ for $\gamma < \gamma_1^{DMS}$ and $d\gamma = \gamma - \gamma_2^{DMS}$ for $\gamma > \gamma_2^{DMS}$, and note that, in contrast to standard snaking, in DMS the left and right saddle-nodes converge to $\gamma_{1,2}^{DMS}$ algebraically as one proceeds up the L_0 branch.¹¹

Defect-mediated snaking is a consequence of the interaction of a heteroclinic cycle $A \rightarrow B \rightarrow A$ with Eckhaus bifurcations of the periodic states B , i.e., with a saddle-center transition of periodic states.^{11,22} This interaction is a consequence of the wavenumber selection process across the pinning region. In systems that are Hamiltonian in space, the wavenumber of the periodic state included in the localized structure is determined by the requirement that the heteroclinic orbits $A \rightarrow B$ and $B \rightarrow A$ lie in a level set of the Hamiltonian.⁹ As a result, the wavenumber varies across the pinning region. We may think of the wavenumber as selected by the fronts on either side of the structure; since the shape of the front varies with the bifurcation parameter r so does the selected wavenumber $k(r)$. In nongradient systems or systems with no spatial Hamiltonian, the process of wavenumber selection is not as well understood. However, it is known that defect-mediated snaking arises when the fronts try to select a wavenumber corresponding to an elliptic periodic state, i.e., a wavenumber lying in the Eckhaus-unstable region. Since no heteroclinic connections, i.e., fronts, can exist in this regime stationary states cannot extend past the transition to Eckhaus instability. As a result, the wavenumber $k^{DMS}(\gamma)$ of the periodic state included in Type-II LS lies on a curve C (solid blue, Fig. 6) in the (γ, k) plane connecting a pair of marginally Eckhaus-unstable states with wavenumbers k_E^\pm . These wavenumbers in turn define the values $\gamma_1^{DMS} < \gamma < \gamma_2^{DMS}$ bounding the pinning region. The curve C

is the same on both the uniform and defect segments of the DMS branch. The figure also shows the family of periodic states parameterized by (γ, k) and bifurcating from (γ^T, k_T) . The upper and lower boundaries of the region of existence of this family of periodic states, hereafter $k^\pm(\gamma)$ (solid red, Fig. 6), represent the two marginally stable wavenumbers associated with the upper equilibrium $A^+(\gamma)$. The upper and lower boundaries of the Eckhaus-stable region will be referred to as $k_E^\pm(\gamma)$ (dashed black, Fig. 6).

A. Type-II time evolution

To study depinning for $\gamma < \gamma_1^{DMS}$ ($\gamma > \gamma_2^{DMS}$), we take a Type-II LS at γ_1^{DMS} (γ_2^{DMS}) as the initial condition and integrate Eq. (2.1) in time. We label the saddle-nodes along L_0 using integers N starting at the bottom, with odd N along $\gamma = \gamma_1^{DMS}$ and even N along $\gamma = \gamma_2^{DMS}$. Thus, smaller (larger) values of N correspond to shorter (longer) structures and we can use N to label the initial condition. Figure 7(a) shows that for $d\gamma < 0$, the periodic pattern may shrink to a stable Type-II LS with fewer rolls; in other cases, the periodic state is eliminated

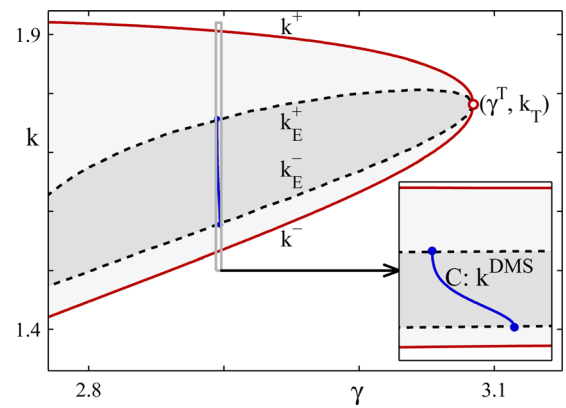


FIG. 6. The family of spatially periodic states parameterized by (γ, k) at $\nu = 7$. Solid red: the marginal stability boundaries $k^\pm(\gamma)$. Dashed black: the Eckhaus stability boundaries $k_E^\pm(\gamma)$. Dark shaded: the Eckhaus stable region (Busse balloon). Light shaded: the Eckhaus unstable regions. Solid blue: the DMS locus $k^{DMS}(\gamma)$.

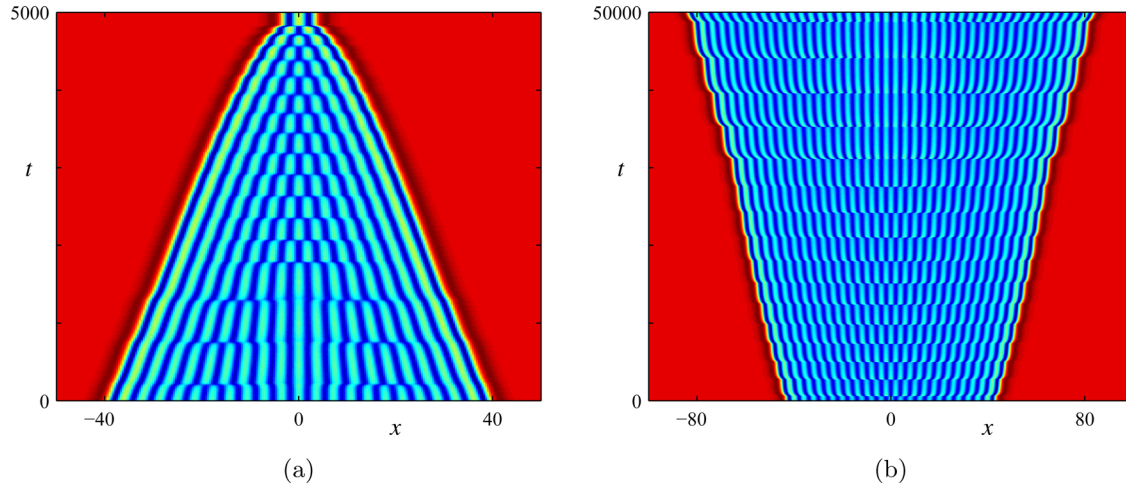


FIG. 7. Space-time plots of $V(x, t)$ showing Type-II LS depinning at (a) $N = 45$, $d\gamma = -1 \times 10^{-3}$; (b) $N = 46$, $d\gamma = 1 \times 10^{-4}$. Reprinted from Ref. 22 with permission from Elsevier.

entirely, leaving the homogeneous state A^- everywhere. In contrast, for $d\gamma > 0$, the periodic pattern expands (Fig. 7(b)) and eventually fills the domain (with appropriate wavelength adjustment in the final stages). In either case, depinning occurs through successive phase slips. At each phase slip, the Type-II LS gains or loses either one roll (on-center depinning) or two rolls (off-center depinning). The figure indicates that on-center depinning is characteristic of relatively short LS, while off-center depinning sets in once the structure becomes sufficiently long.

Figure 7 reveals that for small $|d\gamma|$, the depinning period T depends both on $d\gamma$ and the label N of the nearest saddle-node. This is due in part to the fact that for small N and small $|d\gamma|$, the phase slips take place in the center of the structure (on-center depinning) while for larger N and larger $|d\gamma|$, the central phase slip is replaced by a pair of phase slips symmetrically located on either side of the center (off-center depinning). Figure 8 shows details of on-center and off-center depinning for $\gamma < \gamma_1^{DMS}$. In on-center depinning phase slips are triggered quasistatically and proceed to completion on a timescale that is fast compared to the motion of the front. Thus, the front motion is driven by $d\gamma = \gamma - \gamma_1^{DMS} < 0$ and the phase slips serve to accommodate the speed of the front (Fig. 8(a)). In off-center depinning (Fig. 8(b)), the time evolution is no longer quasistatic. Each phase slip removes one wavelength λ of the pattern while the front moves inward by a distance Λ in the time T between successive phase slips. Since $\lambda > \Lambda$, this implies that the wavelength of the wavetrain must expand to make up the difference. This expansion is clearly visible in Fig. 8(b) and its effect is to push the wavelength of the wavetrain back into the Eckhaus-stable regime. This effect is only visible in the figure because N is small; in broader structures, the wavelength change is smaller and vanishes in the limit $N \rightarrow \infty$. Thus, off-center depinning is the result of a competition between $d\gamma$ and the rate at which phase slips take place. In particular, the (time average of the) expansion speed of the interior wavetrain is given by $(\lambda - \Lambda)/T$, while the (time average of the) front speed is $c = \Lambda/T$.

To quantify these ideas, we let X denote the distance between the phase slip and the front (on either half-domain,

see Fig. 8(b)) and plot the quantities T , Λ , and X as functions of $|d\gamma|$ for $N = 67$ and $N = 72$ to exemplify small N behavior, and $N = 175$ and $N = 162$ to exemplify large N behavior (Fig. 9). Thus both $\gamma < \gamma_1^{DMS}$ (compression) and $\gamma > \gamma_2^{DMS}$ (expansion) are plotted in the same plots. The figure shows that in both cases the depinning period T scales approximately as $|d\gamma|^{-1/2}$ in the on-center case and $|d\gamma|^{-1}$ in the off-center case. The front displacement Λ equals $\pi/k(\gamma_i^{DMS})$, $i = 1, 2$, in the on-center case, doubles to $2\pi/k(\gamma_i^{DMS})$ at the transition point to the off-center case, and varies continuously with further increase in $|d\gamma|$. The distance X between the phase slip and the front is half the width of the LS in the on-center case but decreases sharply at the transition to off-center evolution and approaches 0 for large $|d\gamma|$.

Figure 9 also shows that on-center phase slips persist to relatively large $|d\gamma|$ when N is small (Figs. 9(c) and 9(d)). On the other hand, once $|d\gamma|$ becomes too large, on-center depinning is replaced by off-center depinning and the depinning properties become independent of N . Indeed, in such cases, the depinning state on either half-domain approaches a *pulsating front* state that connects the equilibrium A^- to the periodic state. The pulsating front is similar to defects in oscillatory media considered in the classification of Sandstede and Scheel,²⁸ but we prefer to avoid this terminology since our case violates the genericity assumptions imposed in their work on the asymptotic wavetrains far from the defect. Observe that the pulsating front regime is reached earlier for X than for Λ , because Λ approaches its limiting value only when the wave train defined as the portion between the pair of off-center phase slips consists of a large number of rolls.

In general, the front displacement Λ for a pulsating front is a function $\Lambda(\lambda)$ of the interior wavelength λ . The expansion of the interior wavetrain in Fig. 8(b) changes both λ and Λ . Numerically, we find that this process converges towards an attractor with $\lambda = \Lambda$. The interior wavelength of this attractor, denoted by λ_0 , is independent of the number of rolls on either half-domain, denoted by n . For large n , we can analyze the rate of convergence to this attractor as follows. In one depinning period T , n decreases to $n-1$ and the corresponding interior wavelengths are related by

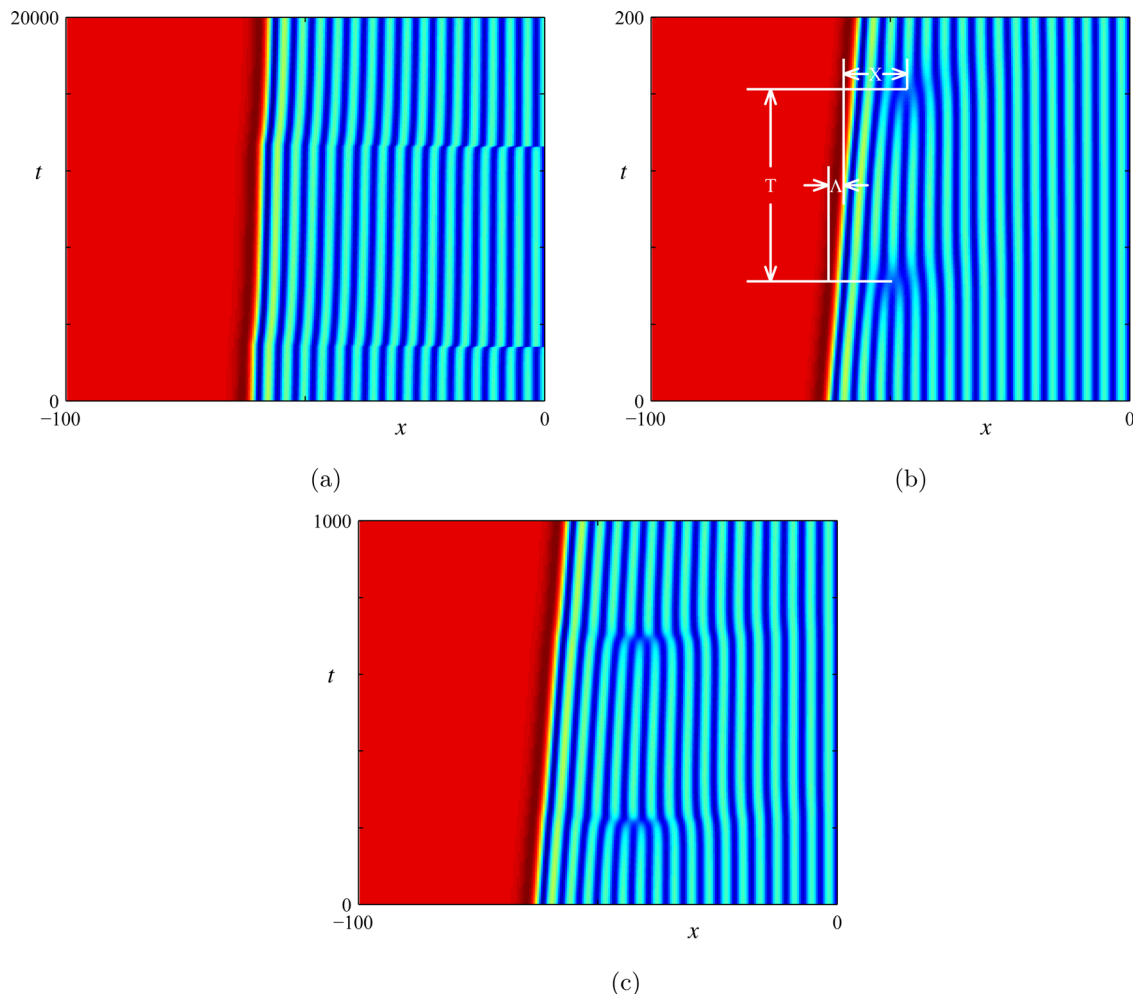


FIG. 8. The first two phase slips during the depinning of Type-II LS, plotted on the left half-domain for $N = 67$. (a) On-center depinning ($d\gamma = -2 \times 10^{-5}$): phase slips take place at the center $x = 0$. (b) Off-center depinning ($d\gamma = -4 \times 10^{-3}$): phase slips take place at a constant distance from the moving front. (c) Intermediate case ($d\gamma = -1 \times 10^{-3}$): phase slips gradually move towards the front. (b) introduces the quantities T , Λ , and X defined in the text.

$$n\lambda_n - (n-1)\lambda_{n-1} = \Lambda(\lambda_n). \quad (4.1)$$

On the other hand, since $\Lambda(\lambda_0) = \lambda_0$ by definition, we have, for $0 < |\lambda_n - \lambda_0| \ll 1$,

$$\Lambda(\lambda_n) - \lambda_0 = \Lambda^{(1)}(\lambda_n - \lambda_0) + h.o.t., \quad (4.2)$$

where $\Lambda^{(1)} \equiv \Lambda'(\lambda_0)$. To leading order, Eqs. (4.1) and (4.2) yield the recurrence relation

$$\frac{\lambda_{n-1} - \lambda_0}{\lambda_n - \lambda_0} = \frac{n - \Lambda^{(1)}}{n - 1}. \quad (4.3)$$

In the asymptotic regime, i.e., for $n > n_0 \gg 1$, Eq. (4.3) can be solved using Mathematica with the result

$$\frac{\lambda_{n_0} - \lambda_0}{\lambda_n - \lambda_0} = n^{1-\Lambda^{(1)}} \left(\frac{\Gamma(n_0)}{\Gamma(1 - \Lambda^{(1)} + n_0)} + O(n^{-1}) \right), \quad (4.4)$$

which takes the form of a scaling law

$$\lambda_n - \lambda_0 \sim n^{\Lambda^{(1)} - 1}. \quad (4.5)$$

The above discussion applies to $d\gamma < 0$; since $\lambda_0 > \lambda > \Lambda$ in Fig. 8(b), it follows that $\Lambda^{(1)} > 1$. The $d\gamma > 0$ case can be

analyzed analogously to yield the same expression as Eq. (4.5), but this time $\Lambda^{(1)} < 1$ because $\lambda > \lambda_0$ and $\lambda > \Lambda$. In either case, both the exponent $\Lambda^{(1)} - 1$ and the asymptotic wavelength λ_0 are functions of γ alone, independent of quantities such as n or λ that characterize the initial condition. Equation (4.2) implies that $\Lambda_n \equiv \Lambda(\lambda_n)$, namely the front displacement during the time the LS contains $2n$ rolls, should obey the same scaling law

$$\Lambda_n - \lambda_0 \sim n^{\Lambda^{(1)} - 1}. \quad (4.6)$$

We remark that similar algebraic approach to an attractor has been studied in other PDEs such as the Burgers equation with small viscosity.⁵

Numerical verification of the scaling law (4.5) or (4.6) involves measurement of λ_n or Λ_n . As depinning occurs, the interior wavetrain responds quasi-statically to front motion, but the sudden wavelength changes caused by phase slips cannot equilibrate instantly within the wavetrain. As a result, the local wavelength near $x = 0$ remains constant for multiple depinning periods in the initial stages of depinning, and in general differs from the average wavelength. Hence, we define the latter as λ_n and plot its variation in time for $d\gamma < 0$ and $d\gamma > 0$ in Fig. 10. For $d\gamma < 0$ ($d\gamma > 0$), λ_n in the initial

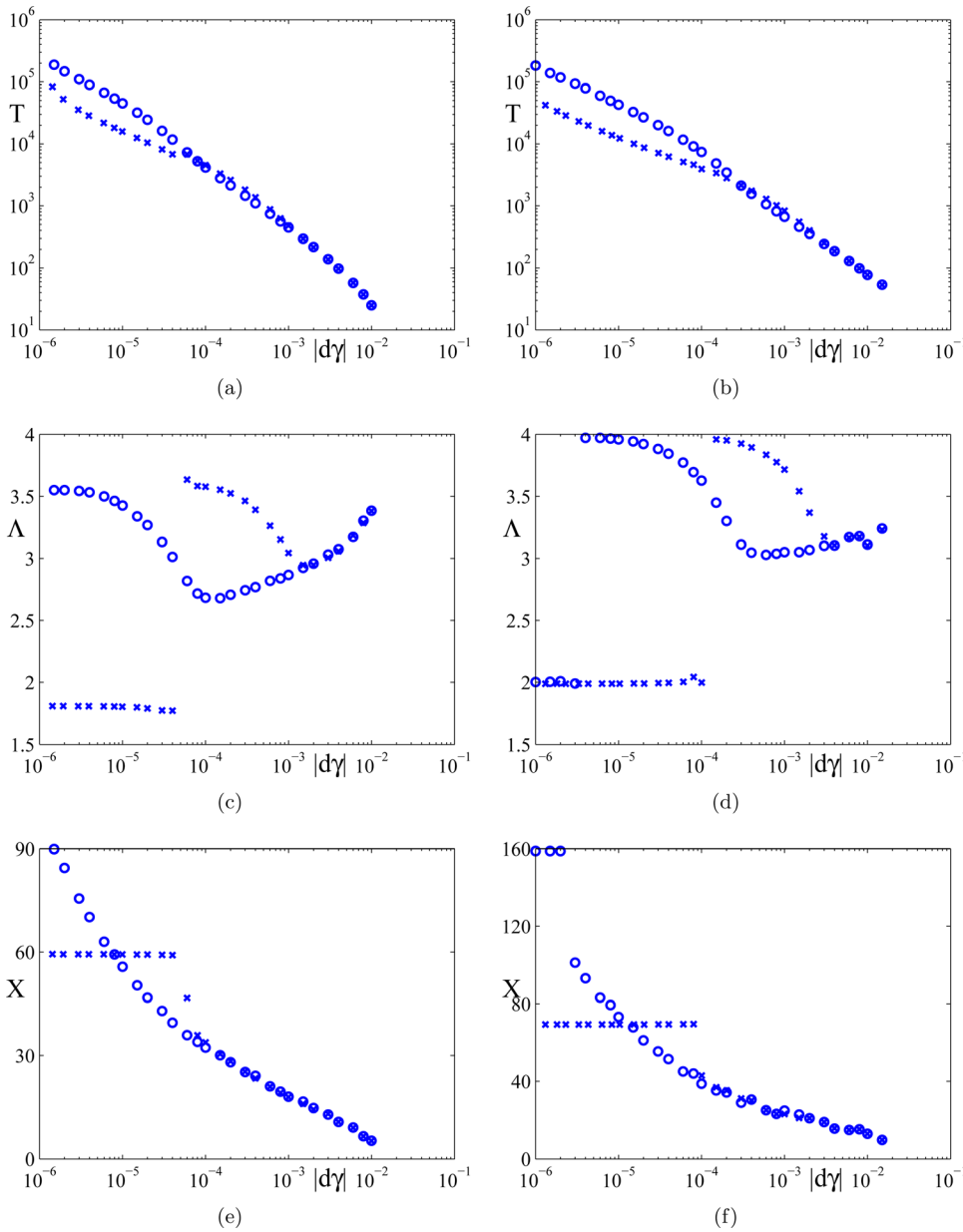


FIG. 9. Plots of the quantities T , Λ , and X defined in Fig. 8(b) as functions of $|d\gamma|$ for ((a), (c), (e)) γ_1^{DMS} (cross; $N = 67$, circle; $N = 175$); ((b), (d), (f)) γ_2^{DMS} (cross; $N = 72$, circle; $N = 162$). The horizontal scale for $|d\gamma|$ is logarithmic. The vertical scale is logarithmic for T but linear for Λ and X .

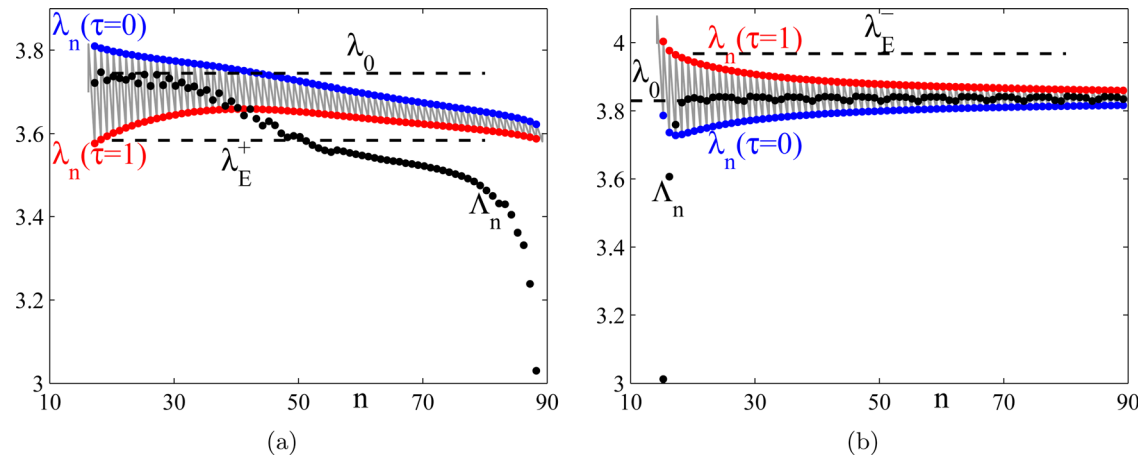


FIG. 10. Plots of the number of rolls n on either half-domain and the interior wavelength λ_n for two depinning processes involving pulsating fronts: (a) $d\gamma = -2 \times 10^{-3}$; (b) $d\gamma = 5 \times 10^{-3}$. As depinning occurs n decreases in (a) and increases in (b). The values of λ_n at the beginning ($\tau = 0$) and at the end ($\tau = 1$) of each depinning period are highlighted. The front displacement Λ_n in each depinning period is shown for comparison; the marginally Eckhaus-stable wavelength λ_E^\pm and the asymptotic wavelength λ_0 are also indicated.

condition is chosen close to the marginally Eckhaus-stable wavelength λ_E^+ (λ_E^-), where $\lambda_E^\pm \equiv 2\pi/k_E^\pm$. Subsequently, n remains constant in each depinning period and decreases (increases) by 1 at each phase slip. For fixed n , we introduce the rescaled time τ such that $\tau = 0$ and $\tau = 1$, respectively, denote the times of the previous and next phase slips. The front displacement Λ_n in Fig. 10 is measured between $\tau = 0$ and $\tau = 1$ as in Fig. 8(b). As shown in Fig. 10, the wavelength change $|\lambda_n(\tau = 1) - \lambda_n(\tau = 0)| = \Lambda_n/n$ caused by the front motion generally increases as n decreases. Thus Eq. (4.5) is expected to hold only at suitably chosen times $\tau = \tau_n \in (0, 1)$ that cannot be determined *a priori*. However, the scaling behavior of Λ_n should be largely independent of τ_n since $\Lambda_n(\tau = 1) = \Lambda_{n\pm 1}(\tau = 0)$ for $d\gamma \gtrless 0$. As shown in Fig. 10, initially the variation of Λ_n is indeed consistent with Eq. (4.6) with exponent $|\Lambda^{(1)} - 1| > 1$. In the $d\gamma > 0$ case, Λ_n approaches λ_0 rapidly because $n_0 \equiv n(t = 0)$ is small. In the $d\gamma < 0$ case, however, n_0 is large and Λ_n approaches λ_0 slowly in a “piecewise smooth” fashion. For both $d\gamma > 0$ and $d\gamma < 0$, the asymptotic wavelength λ_0 dynamically selected by the pulsating front is strongly Eckhaus-stable. Moreover, as λ_0 is approached, namely, as n increases for $d\gamma > 0$ and as n decreases for $d\gamma < 0$, Λ_n does not remain constant but

oscillates around λ_0 . In the former case, the dominant frequency is $f_{\text{peak}} \approx 0.18$, which corresponds to a dominant period $T_{\text{peak}} \approx 5.6$; in addition, there is a subdominant frequency at $2f_{\text{peak}}$ with a power spectrum density (PSD) about 27% of the peak value. In the latter case, the PSD peaks around frequency 1/2, namely, the highest resolvable frequency. In this situation, the dominant period is generally undetermined owing to aliasing. In addition, the PSD remains nonzero at frequency 1/2, suggesting a need for a longer series of data points to reveal periodicity. In view of the relation $c_n = \Lambda_n/T_n$, we have also examined the variation of c_n and T_n as functions of n . For both $d\gamma < 0$ and $d\gamma > 0$, we find that c_n remains almost constant over the entire range of n , but the periodic fluctuation of Λ_n near λ_0 is present for both c_n and T_n .

We now examine the depinning process for long structures in a reference frame that is comoving with the front. Figure 11(a) shows a space-time plot corresponding to a structure that is contracting while Fig. 11(b) shows the corresponding plot for an expanding structure. In both cases, only the region close to the front is shown. In both cases, repeated phase slips take place at a fixed location separated from a sharp front by several more or less stationary rolls, and

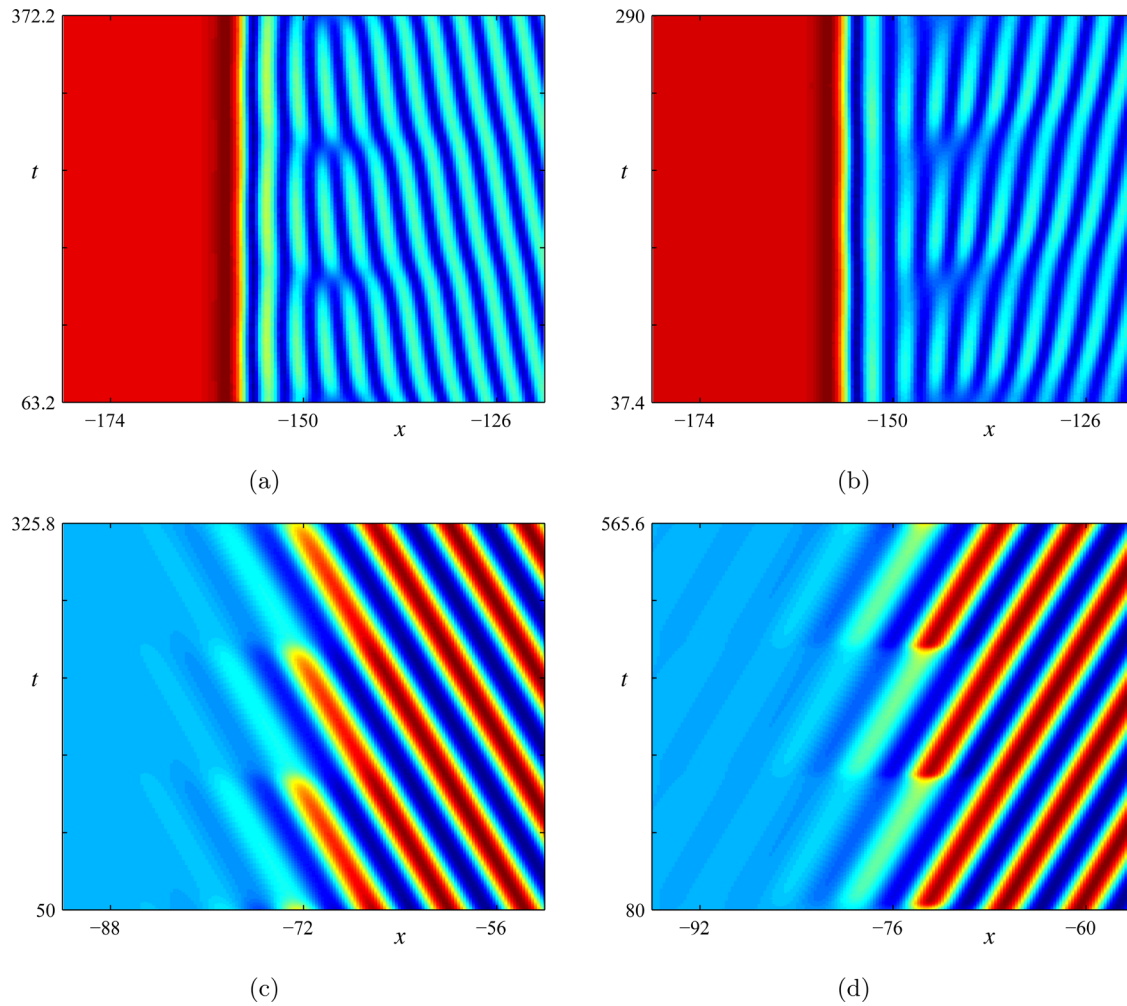


FIG. 11. Off-center depinning of a Type-II LS as a pulsating front. In each case, the space-time plot is drawn in a frame comoving with the front. (a) Sink in the 1:1 FCGLE (2.1) at $d\gamma = -4 \times 10^{-3}$; (b) source in Eq. (2.1) at $d\gamma = 1 \times 10^{-2}$; (c) sink in SH23 (4.7); (d) source in Eq. (4.7). Depinning is shown for (c) $r = -0.3410$ and (d) $r = -0.2580$ at fixed $b_2 = 1.8$. The snaking region of steady Type-II LS in SH23 is $r \in [-0.3390, -0.2593]$.

separating the standing structure near the front from the incoming wave (Fig. 11(a)) or the outgoing wave (Fig. 11(b)). In the former (latter), the result is a stationary but time-periodic sink (source) at a fixed distance from the front. As a result, the structure shown in Fig. 11(a) resembles an interaction between a fixed boundary and an incident finite amplitude traveling wave in a system with a preferred direction of propagation, i.e., in a system with broken reflection symmetry.³⁰ In such systems, reflected waves are necessarily evanescent, and a standing structure therefore only forms near the boundary, requiring the presence of phase slips to eliminate incoming phase. Similar behavior governs the source of phase as shown in Fig. 11(b). However, phase may be removed in another way as well, and that is via a *soft* front (Fig. 11(c)), in which the amplitude of the incoming wave drops gradually and smoothly to zero, where the phase becomes undefined. In this case, phase slips are no longer required. Figure 11(d) shows an example of the left portion of an expanding structure in the Swift-Hohenberg equation with competing quadratic and cubic nonlinearities (SH23),

$$u_t = [r - (1 + \partial_{xx})^2]u + b_2 u^2 - u^3, \quad (4.7)$$

again in a frame moving with the expanding front. Here, the amplitude of the traveling wave builds up gradually with increasing x , leading to a source of waves whose structure can be understood in terms of a spatially growing front. However, in contrast to similar structures present, for example, in the complex Ginzburg-Landau equation with drift,³⁰ in the present case, the front always propagates into a *stable* state (such a front is *pushed* in the terminology of Ref. 33), and hence its properties cannot be described in terms of the transition to absolute instability in the moving frame.⁸

When the wavenumber k is far from the Eckhaus boundary, the instability develops rapidly as shown in Fig. 12(a). This Type-II LS includes a strongly Eckhaus-unstable periodic state and evolves via a gradual invasion of the unstable wave train by a stable one with a different wavenumber. This process is mediated by a series of phase slips that start near the pair of bounding fronts and migrate towards the center until the unstable wave train is completely replaced by a

stable wavetrain. The pair of invasion fronts formed by these phase slips may be regarded as a generalization of a pair of pulled fronts³³ through which a stable periodic state invades a Turing-unstable equilibrium. Figure 12(b) shows an example of the latter, the depinning of a Type-I LS at $\gamma = 2.87 < \gamma_1^{DMS}$. The figure reveals that the rate at which the inner structure shrinks increases as the Turing instability drives A^+ to a periodic state.

B. Analysis of Type-II depinning

Figure 13(a) shows the front speed $c^H(\gamma)$ obtained from direct numerical simulation of Type-II depinning (crosses). The behavior of $c^H(\gamma)$ follows remarkably closely the behavior of $c^I(\gamma)$ obtained by computing heteroclinic orbits \mathbb{H} in Eq. (3.2) connecting A^\pm (solid line). In this section, we explore the relation between these two quite distinct calculations.

The enlargement in Fig. 13(a) indicates that the situation is now quite different from that encountered in Fig. 3. First of all, the Turing bifurcation now occurs at $\gamma^T > \gamma_-^{SN}$ implying that A^+ is elliptic throughout the region of bistability (dotted-dashed line). Second, the locus of $c^I(\gamma)$ (solid line) appears to cross this region. Since this is not possible, we provide in Fig. 13(a) an enlargement of the “crossing” region. We see that the heteroclinic connections \mathbb{H}^+ approaching $c^I = 0$ from above converge to a limit that agrees very well with the numerically determined lower limit γ_1^{DMS} for defect-mediated snaking; likewise the heteroclinic connections \mathbb{H}^- approaching $c^I = 0$ from below converge to a limit that agrees very well with the numerically determined upper limit γ_2^{DMS} . These results confirm that the analysis of the heteroclinic orbits \mathbb{H} in Eq. (3.2) allows us to identify the DMS snaking region, at least when the amplitude of the oscillations within the Type-II LS is not too large.

To understand why, we first observe that the conditions for a reversibility-breaking bifurcation on A^+ as c varies at fixed γ are satisfied throughout the bistability region (see Appendix A), with larger wavenumbers in the left half-plane for $c > 0$ and the right half-plane for $c < 0$, and vice versa for the smaller wavenumbers. Moreover, the sign and magnitude

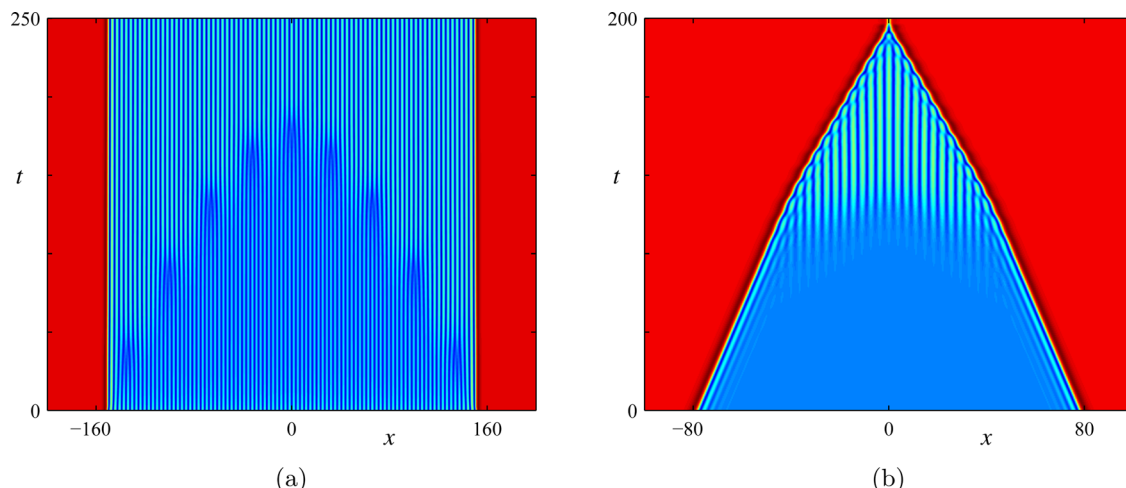


FIG. 12. Space-time plot of $V(x, t)$ showing the time evolution of (a) a Type-II LS at $(\gamma, k) = (2.8947, 1.85)$; (b) a Type-I LS at $\gamma = 2.87$.

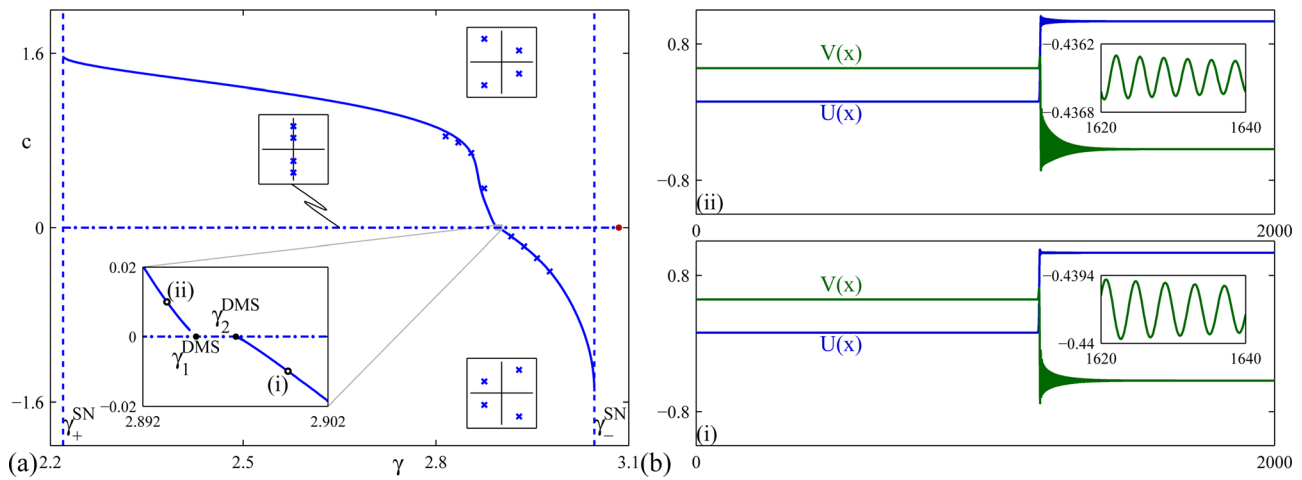


FIG. 13. (a) Plot of the front speed c as a function of γ at $\nu = 7$. Crosses: DNS of Eq. (2.1) for depinning of Type-II LS. Solid line: continuation of heteroclinic orbits in Eq. (3.2). Dashed: SN bifurcations (left/right: γ_{\pm}^{SN}). Dotted-dashed: RB bifurcations on A^+ . (b) Front profiles at (i) $c = -0.01$; (ii) $c = 0.01$. The insets show that the tail wavenumber in (ii) is larger than (i), consistent with the stable eigenvalues of A^+ depicted in (a).

of c also determine the decay rate of the oscillations corresponding to solutions of Eq. (3.2) in the left half-plane. As \mathbb{H}^+ approaches the elliptic region from above, the decay rate of the oscillations decreases towards zero implying that in the limit (i.e., $\gamma \rightarrow \gamma_1^{DMS}$) \mathbb{H}^+ approaches a connection to an “infinitesimal” periodic wavetrain. This is a delicate situation²¹ but fortunately for our purposes, it suffices to know that for $\gamma > \gamma_1^{DMS}$ there are no connections of type \mathbb{H}^+ between A^- and A^+ and likewise for \mathbb{H}^- in $\gamma < \gamma_2^{DMS}$. Figure 13(b) shows typical \mathbb{H}^\pm for small values of c' . Thus provided the oscillation amplitude within the Type-II LS is small, the limit points of \mathbb{H}^\pm provide a good approximation to $\gamma_{1,2}^{DMS}$.

Near $\gamma = \gamma_{1,2}^{DMS}$, the depinning process can be studied following similar work on depinning in the Swift-Hohenberg equation.^{8,9} We suppose that the time T taken to travel from the vicinity of one saddle-node to the one immediately above (expanding front) or below (contracting front) scales as $T \sim |d\gamma|^{-1/2}$, where $|d\gamma|$ is the distance from the boundary of the DMS pinning region. In this regime, we can predict the constant of proportionality $\tau \equiv T/|d\gamma|^{-1/2}$ from weakly nonlinear theory. We let $A_0(x) \equiv (U_0(x), V_0(x))$ be a particular even parity stationary LS at γ_i^{DMS} , $i=1, 2$, and define $|d\gamma| \equiv |\gamma - \gamma_i^{DMS}|$. For $|d\gamma| \ll 1$, we have

$$\begin{bmatrix} U(x,t) \\ V(x,t) \end{bmatrix} = \begin{bmatrix} U_0(x) \\ V_0(x) \end{bmatrix} + |d\gamma|^{1/2} \begin{bmatrix} U_1(x,t) \\ V_1(x,t) \end{bmatrix} + |d\gamma| \begin{bmatrix} U_2(x,t) \\ V_2(x,t) \end{bmatrix} + O(|d\gamma|^{3/2}). \quad (4.8)$$

The time scale on which perturbations evolve is $|d\gamma|^{-1/2}$. It follows from Eq. (2.2) that

$$\begin{aligned} \mathcal{L} \left(\begin{bmatrix} U_1 \\ V_1 \end{bmatrix} + |d\gamma|^{1/2} \begin{bmatrix} U_2 \\ V_2 \end{bmatrix} \right) \\ = \partial_t \begin{bmatrix} U_1 \\ V_1 \end{bmatrix} + |d\gamma|^{1/2} \left(\begin{bmatrix} 1 & -\beta \\ \beta & 1 \end{bmatrix} \begin{bmatrix} 3U_0^2 + V_0^2 & 2U_0V_0 \\ 2U_0V_0 & U_0^2 + 3V_0^2 \end{bmatrix} \right. \\ \times \left. \begin{bmatrix} U_0 \\ V_0 \end{bmatrix} - \begin{bmatrix} \text{sgn}(d\gamma) \\ 0 \end{bmatrix} \right) + O(d\gamma), \quad (4.9) \end{aligned}$$

where \mathcal{L} is the linearized FCGL operator evaluated at γ_i^{DMS} ,

$$\mathcal{L} = \begin{bmatrix} \mu & -\nu \\ \nu & \mu \end{bmatrix} + \begin{bmatrix} 1 & -\alpha \\ \alpha & 1 \end{bmatrix} \partial_{xx} - \begin{bmatrix} 1 & -\beta \\ \beta & 1 \end{bmatrix} \begin{bmatrix} 3U_0^2 + V_0^2 & 2U_0V_0 \\ 2U_0V_0 & U_0^2 + 3V_0^2 \end{bmatrix}, \quad (4.10)$$

and the first term on the right side of Eq. (4.9) is formally of order $|d\gamma|^{1/2}$. We require that the perturbations (U_j, V_j) , $j \geq 1$, decay to 0 as $x \rightarrow \pm\infty$.

At leading order in $|d\gamma|^{1/2}$, we solve

$$\mathcal{L} \begin{bmatrix} U_1 \\ V_1 \end{bmatrix} = 0, \quad (4.11)$$

subject to the requirement $(U_1, V_1) \rightarrow 0$ as $x \rightarrow \pm\infty$. The solution of this problem determines the null eigenvector(s) of \mathcal{L} and these completely determine the dynamics near the saddle-node. These eigenvectors are either odd or even under reflection $x \rightarrow -x$, with the odd mode corresponding to the neutrally stable Goldstone mode while the even mode corresponds to an amplitude mode whose growth rate passes through zero at the saddle-node. Since the latter mode is involved in the depinning process, it is important to understand the behavior of this mode near the left and right saddle-nodes. Figures 14(a) and 14(b) show this mode on the uniform segment of the DMS branch near the saddle-node. In contrast to the amplitude mode involved in front depinning in the Swift-Hohenberg equation the amplitude mode in the present case is spatially extended. This is a consequence of the fact that the saddle-nodes on the DMS branch are associated with Eckhaus instability of the periodic state: DMS is only possible in the interval $(\gamma_1^{DMS}, \gamma_2^{DMS})$ in which the periodic state with wavenumber $k(\gamma)$ is hyperbolic (Fig. 6), and the Eckhaus instability forming the boundary of this region is associated with a spatially extended eigenfunction. In the following, we refer to this mode as the Eckhaus mode $A_E(x)$; its growth rate $\sigma_E < 0$ depends on $d\gamma$ as $\sigma_E = f_E |d\gamma|^{1/2}$ (Figs. 15(a) and 15(b)), where $f_E < 0$ is a constant that depends on the label N of the particular saddle-node.

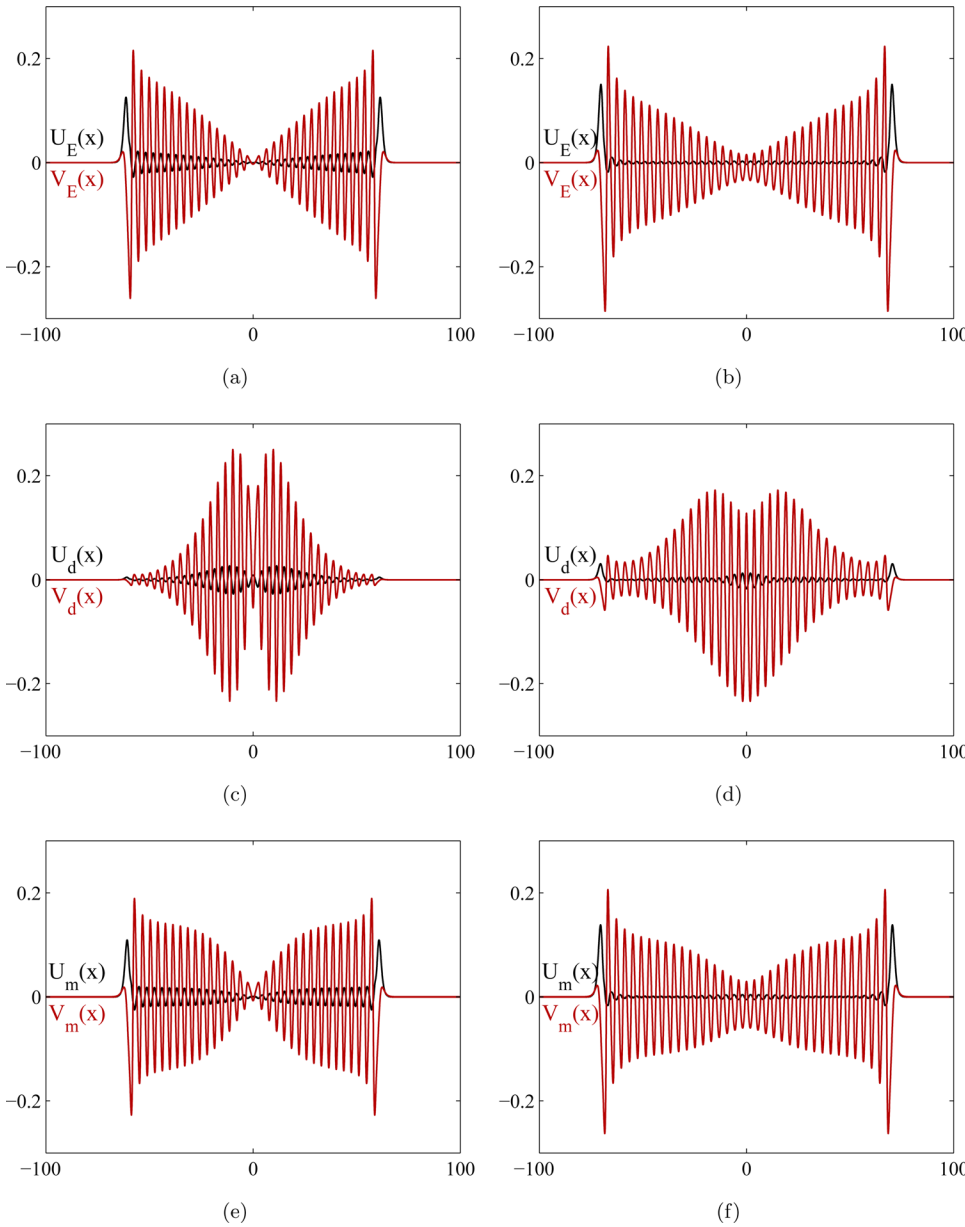


FIG. 14. The Eckhaus, defect, and mixed modes ($A_E(x)$, $A_d(x)$, and $A_m(x)$) at ((a), (c), (e)) $N = 67$; ((b), (d), (f)) $N = 72$. The Eckhaus and defect modes are computed at $|d\gamma| = 2 \times 10^{-5}$.

Near the saddle-node on the defect segment, the amplitude mode takes a very different form. This is a consequence of the fact that on this branch the LS no longer takes the form of a uniform amplitude wavetrain embedded in an A^- background. As a result, the near-marginal eigenfunction becomes localized near the defect in the center of the LS. We refer to the resulting mode as the defect mode $A_d(x)$. Its growth rate $\sigma_d > 0$ depends on $d\gamma$ approximately as $\sigma_d = f_d |d\gamma|$ (Figs. 15(c) and 15(d)), where $f_d > 0$ is a constant almost independent of N . This is evidently a consequence of the fact that this mode is dominated by the central defect rather than the proximity to the saddle-node and the associated Eckhaus instability. Nonetheless, we anticipate that the expected square-root behavior of the growth rate σ_d is restored very close to the saddle-node. Indeed, the $A_E(x)$ and $A_d(x)$ modes turn into one another at either saddle-node despite their very different appearance on either side of it. The marginally stable even parity mode at this location is shown

in Figs. 14(e) and 14(f) and will be called a mixed mode $A_m(x)$. Its growth rate is $\sigma_m = 0$ by construction.

The profile of the Eckhaus mode $A_E(x)$ can be constructed as follows. Introducing the shorthand $k \equiv k^{DMS}(\gamma)$ and $k_i^{DMS} \equiv k^{DMS}(\gamma_i^{DMS})$, we observe from Fig. 6 that $|dk| \equiv |k - k_i^{DMS}| \sim |d\gamma|^{1/2}$ for $|d\gamma| \ll 1$. This behavior is a consequence of the (numerical) observation that the amplitude of the wavetrain determines uniquely its wavenumber k . This wavenumber selection process is well understood in time-independent systems that are Hamiltonian in space (such as the Swift-Hohenberg equation^{9,10}) and is a consequence of the presence of the fronts connecting the wavetrain to the background state A^- . Thus, a saddle-node bifurcation in the wavenumber (Fig. 6). We write the steady LS at γ near γ_i^{DMS} as a connection between the background state A^- and a periodic state P and back again,

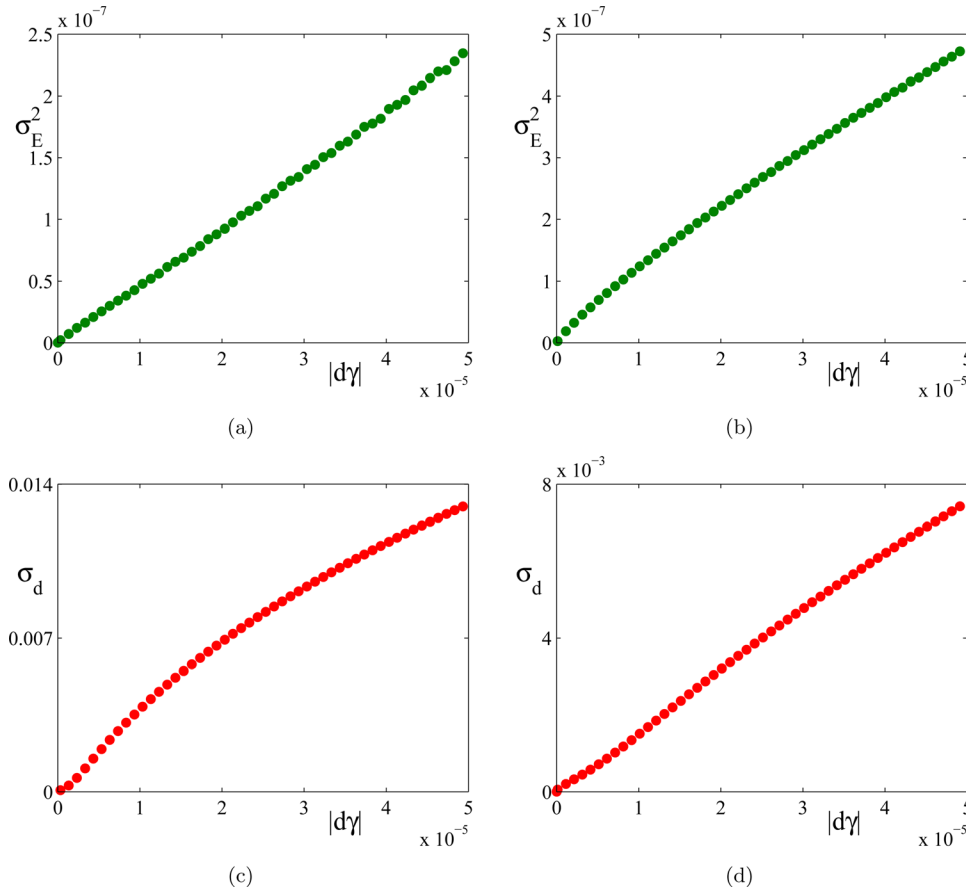


FIG. 15. Growth rates of the Eckhaus and defect modes (σ_E and σ_d) as functions of $|d\gamma|$ at ((a), (c)) $N = 67$; ((b), (d)) $N = 72$.

$$A(x; k) \equiv A^- \xrightarrow{F(-n\pi - kx; k)} P(kx - 2m\pi, k) \xrightarrow{F(kx - n\pi; k)} A^-, \quad (4.12)$$

where F (P) denotes the front (roll) profile (P is even and 2π -periodic in the first argument), n denotes the total number of rolls, and m ranges from $-n/2$ to $n/2$. In Eq. (4.12), the parametric dependence on k has been kept, but terms at $O(d\gamma)$ or higher orders have been discarded. Differentiating with respect to k for each x , we get an eigenfunction homoclinic to zero

$$\frac{dA(x; k)}{dk} = 0 \xrightarrow{-xF' + F_k} xP' + P_k \xrightarrow{xF' + F_k} 0, \quad (4.13)$$

where ' and the subscript k denote, respectively, partial derivatives with respect to the first argument and with respect to k . Modulo normalization, Eq. (4.13), yields the Eckhaus mode $A_E(x)$. We see that along the uniform segment $A_E(x) = xP' + P_k \neq 0$, with the xP' term responsible for the linear change in the amplitude of the mode with x visible in Figs. 14(a) and 14(b). These figures thus confirm the Eckhaus nature of this mode. Incidentally, the same scaling law, $|dk| \sim |d\gamma|^{1/2}$, also applies to homoclinic snaking in the 2:1 FCGLE (Fig. 3 of Ref. 22), where the selected wavenumbers $k(\gamma)$ form a closed curve in the (γ, k) plane (Fig. 5 of Ref. 22). In this case, the Eckhaus mode must also take the form (4.13). In contrast, for homoclinic snaking in the Swift-Hohenberg equation,⁹ the wavenumber variation on the LS

branch above and below the saddle-node is identical. Thus, $|dk| \sim |d\gamma|$ and hence $P' = 0$, i.e., the associated amplitude mode vanishes on the wavetrain and remains localized at the pair of fronts as computed in Ref. 9.

As we have seen the Eckhaus mode on the uniform amplitude segment changes rapidly and dramatically when one passes the saddle-node and moves onto the defect portion of the DMS branch. This fact greatly complicates the calculation of the depinning speed and implies that one cannot compute the front speed by simply projecting Eq. (2.2) onto the marginal eigenfunction (U_m, V_m) . Instead, we proceed as in Refs. 2, 9, and 10 but allow for a general superposition of near-marginal modes

$$\begin{bmatrix} U_1(x, t) \\ V_1(x, t) \end{bmatrix} = \sum_j a_j(t) \begin{bmatrix} U_j(x) \\ V_j(x) \end{bmatrix}, \quad (4.14)$$

where $a_j(t)$ are slowly evolving real amplitudes and the summation index j ranges over a subset of $\{E, d, m\}$.

With this approximate solution of Eq. (4.11), we now proceed to $O(d\gamma)$ and solve

$$\begin{aligned} \mathcal{L} \begin{bmatrix} U_2 \\ V_2 \end{bmatrix} &= \partial_t \begin{bmatrix} U_1 \\ V_1 \end{bmatrix} + |d\gamma|^{1/2} \left(\begin{bmatrix} 1 & -\beta \\ \beta & 1 \end{bmatrix} \right. \\ &\quad \times \left. \begin{bmatrix} 3U_1^2 + V_1^2 & 2U_1V_1 \\ 2U_1V_1 & U_1^2 + 3V_1^2 \end{bmatrix} \begin{bmatrix} U_0 \\ V_0 \end{bmatrix} - \begin{bmatrix} \text{sgn}(d\gamma) \\ 0 \end{bmatrix} \right). \end{aligned} \quad (4.15)$$

The solvability condition for this equation requires that the right side is orthogonal to all null eigenvectors of $\mathcal{L}^\dagger = \mathcal{L}^T$,

resulting in the following set of ODEs for the amplitudes $a_j(t)$:

$$\sum_j \alpha_l^j \frac{da_j}{dt} = |d\gamma|^{1/2} \left(\beta_l \text{sgn}(d\gamma) + \sum_j \beta_l^j a_j^2 + \sum_h \sum_{j < h} \beta_l^{h,j} a_h a_j \right). \quad (4.16)$$

Here, the α and β coefficients are (the integration limits are always $\pm\infty$)

$$\alpha_l^j \equiv \int (U_l^\dagger U_j + V_l^\dagger V_j) dx, \quad \beta_l \equiv \int U_l^\dagger dx, \quad (4.17)$$

$$\beta_l^j \equiv - \int [U_l^\dagger \ V_l^\dagger] \begin{bmatrix} 1 & -\beta \\ \beta & 1 \end{bmatrix} \begin{bmatrix} 3U_j^2 + V_j^2 & 2U_j V_j \\ 2U_j V_j & U_j^2 + 3V_j^2 \end{bmatrix} \begin{bmatrix} U_0 \\ V_0 \end{bmatrix} dx, \quad (4.18)$$

$$\begin{aligned} \beta_l^{h,j} \equiv & -2 \int [U_l^\dagger \ V_l^\dagger] \begin{bmatrix} 1 & -\beta \\ \beta & 1 \end{bmatrix} \\ & \times \begin{bmatrix} 3U_h U_j + V_h V_j & U_h V_j + U_j V_h \\ U_h V_j + U_j V_h & U_h U_j + 3V_h V_j \end{bmatrix} \begin{bmatrix} U_0 \\ V_0 \end{bmatrix} dx. \end{aligned} \quad (4.19)$$

We find that the linear combination of all three modes fits the computed quantity $A(x, t) - A_0(x)$ well with $A_0(x)$ evaluated right at γ_i^{DMS} . However, since the depinning of the front is linked to phase slips triggered by the Eckhaus instability, we neglect the contributions from A_m and A_d and evaluate the above integrals numerically. The signs of $A_E(x)$ and $A_E^\dagger(x)$ are chosen such that $\alpha_E^E > 0$. When Eq. (4.16) describes depinning, the signs of the other coefficients are $d\gamma < 0$ and $\beta_E \beta_E^E < 0$ for $\gamma = \gamma_1^{\text{DMS}}$, and $d\gamma > 0$ and $\beta_E \beta_E^E > 0$ for $\gamma = \gamma_2^{\text{DMS}}$. By construction the amplitude function $a_E(t) = -\infty$ right after the first phase slip, and we postulate that $a_E(t) = 0$ right before the second phase slip since at this moment $A(x, t)$ is expected to be marginally Eckhaus-unstable and thus should coincide with $A_0(x)$. In either case, Eq. (4.16) has no fixed point and $a_E(t)$ passes from $-\infty$ to 0 in the finite time

$$T = \frac{\pi \alpha_E^E}{2(\beta_E \beta_E^E d\gamma)^{1/2}}. \quad (4.20)$$

In practice, we find that the integral β_E^E tends towards zero as N increases. It is hard to attain the level of precision in the computation of the eigenfunctions $A_E(x)$ and $A_E^\dagger(x)$ required to evaluate this integral, so instead we express T in terms of the eigenvalue σ_E , which is numerically more reliable. When Eq. (4.16) describes steady states, the sign of $d\gamma$ is opposite to that for depinning while the other coefficients remain the same. In this case, Eq. (4.16) has the following pair of fixed points with eigenvalues:

$$a_E^0 = \pm \text{sgn}(\beta_E^E) \left(\frac{\beta_E \text{sgn}(d\gamma)}{\beta_E^E} \right)^{1/2} \quad \text{with} \quad \sigma_E = \pm \frac{2(\beta_E \beta_E^E d\gamma)^{1/2}}{\alpha_E^E}. \quad (4.21)$$

The lower sign corresponds to steady states on the uniform segment for which the growth rate σ_E of the Eckhaus mode

$A_E(x)$ is negative. It then follows from Eqs. (4.20) and (4.21) that the predicted relation between T and σ_E is

$$T = \frac{\pi}{|\sigma_E|}. \quad (4.22)$$

To test this result, we postulate a relation between T and $|d\gamma|$ of the form

$$\frac{1}{T^2} = m(|d\gamma| - \tilde{\gamma}) \quad (4.23)$$

and determine the slope m and the intercept $\tilde{\gamma}$ (both as functions of N) from DNS of Eq. (2.1). (In Fig. 22 of Ref. 22, the fold labels have been overcounted by 2.) The results are compared with the predicted values $m = f_E^2/\pi^2$ and $\tilde{\gamma} = 0$ that follow from Eq. (4.22). As shown in Fig. 16, for γ_1^{DMS} (panel (a)) the actual and predicted slopes m agree almost perfectly, while for γ_2^{DMS} (panel (b)), the predicted m is larger than the actual value, or equivalently the predicted depinning period T is shorter than the actual period. Aside from this discrepancy, we find in DNS of Eq. (2.1) that the prediction (4.23) fails for very small $|d\gamma|$ and more generally that the intercept $\tilde{\gamma}$ does not vanish. It is precisely in this regime that the marginal mode A_m should be employed. As shown in Fig. 16, for γ_2^{DMS} (panel (d)) $\tilde{\gamma}$ depends on N periodically. The dominant frequency is $f_{\text{peak}} \approx 0.045$, which corresponds to a dominant period $T_{\text{peak}} \approx 22$. Interestingly this period is consistent with the period of Λ_n in Fig. 10(b) since n increases by 1 when N increases by 4. For γ_1^{DMS} (panel (c)), this dependence looks random, but its Fourier transform again suggests periodicity with the dominant frequency $f_{\text{peak}} \approx 0.21$.

V. DISCUSSION

In this paper, we studied the depinning of Type-I and Type-II localized structures in forced dissipative systems using a combination of direct numerical simulations and semianalytical theory. In both cases, the depinning process leads to the propagation of a front into a stable background state. Thus, the front speed is determined by nonlinear processes and the fronts are *pushed*.

We focused on the forced complex Ginzburg-Landau equation with 1:1 resonance as an example of a system with nonvariational dynamics in which earlier work²² identified a new type of homoclinic snaking that has been called defect-mediated snaking. Associated with this structure of the pinning region is a new type of depinning we have labeled Type-II depinning. In this depinning process, the front motion triggers phase slips behind the front that allow the front to continue its motion. We have demonstrated that the phase slips are not passive. As a result, the front motion is driven by a combination of factors: the distance from the edge of the pinning region and the rate at which phase can slip behind the front. The analysis of the resulting front motion is complicated by the fact that the time from the triggering of the Eckhaus instability by the compression/expansion of the wavelength to a completed phase slip is imperfectly known. This time is dominated by the (presumably small) amplitude

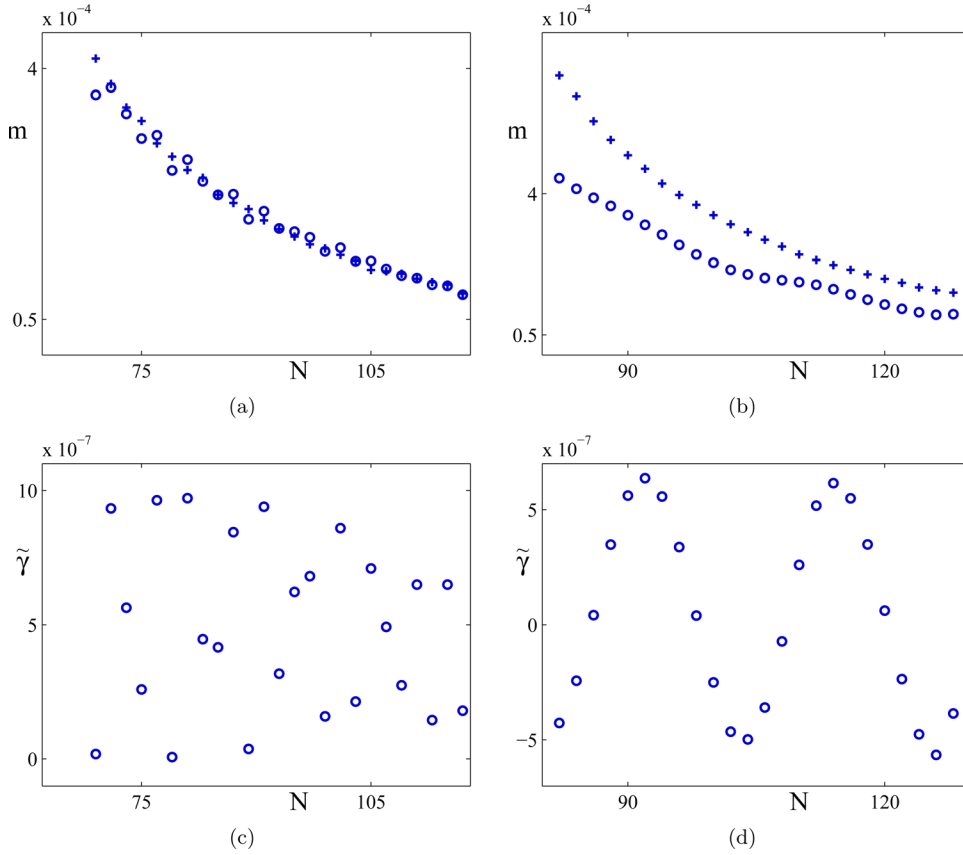


FIG. 16. The slope m and intercept $\tilde{\gamma}$ in Eq. (4.23) as functions of N for (a) and (c) γ_1^{DMS} and (b) and (d) γ_2^{DMS} . “o”: DNS; “+”: weakly nonlinear theory.

of the initial perturbation and is therefore determined by the inverse growth rate of the instability. Despite this uncertainty, we have been able to obtain theoretical predictions that are in good agreement with the DNS results. However, further progress requires a better understanding of the time it takes for a phase slip to occur as a function of the distance from the Eckhaus boundary. We have also demonstrated that the width of the pinning region in DMS is well approximated by the zero speed limit of heteroclinic connections between the background state A^- and the *homogeneous* state A^+ , a fact that we have ascribed to the relatively small amplitude of the oscillations included in the Type-II LS we study. This observation is potentially significant since it allows a semianalytical determination of the width of the pinning or snaking region.

It is tempting to try to relate the dynamics we have observed to those found in systems defined on growing domains, such as in the recent work of Ueda and Nishiura.³¹ In this and related work, the problem is mapped onto a domain of fixed size using a time-dependent rescaling of the spatial variable x and the resulting problem is solved subject to periodic or Neumann boundary conditions. As a result the domain growth affects only the diffusion coefficients and its effect is distributed *evenly* throughout the domain. Thus if one cell splits so does every other cell. In our system, the presence of fronts on either side introduces amplitude (and wavelength) modulation into the pattern and this modulation is in turn responsible for selecting preferred locations for the phase slips. As a result, the constituent cells are in fact heterogeneous and the system evolves in a distinct way, as documented in the present paper. We anticipate that in the presence of non-Neumann boundary conditions, the repeated

splitting observed by Ueda and Nishiura in their study of the Gray-Scott model may also change drastically and will report on this topic in the near future.

The present work is a contribution to the theory of dynamical wavelength selection mediated by front invasion. This is a fundamentally nonequilibrium process, and the wavelength that is selected may well be unstable to subsequent instabilities that move the selected structure closer to equilibrium. This can happen with both pulled fronts when these invade a linearly stable state and in pushed fronts as here.¹⁰ It remains a topic of considerable theoretical interest.

ACKNOWLEDGMENTS

This work was supported by the National Science Foundation under grants DMS-0908102 (Y.M. and E.K.) and DMS-0940261 (Y.M.).

APPENDIX A: MOVEMENT OF EIGENVALUES FOR THE RB BIFURCATION

Let $A_0 \equiv U_0 + iV_0$ be an equilibrium solution to Eq. (3.2) and denote $R_2 \equiv U_0^2 + V_0^2$. Linearizing around A_0 , we obtain the following equation for the spatial eigenvalues λ :

$$(1 + \alpha^2)\lambda^4 + 2c\lambda^3 + (2M + c^2)\lambda^2 + 2cN\lambda + Q = 0, \quad (\text{A1})$$

where

$$M = \mu + \alpha\nu - 2(1 + \alpha\beta)R_2, \quad N = \mu - 2R_2, \quad (\text{A2})$$

$$Q = \mu^2 + \nu^2 - 4(\mu + \beta\nu)R_2 + 3(1 + \beta^2)R_2^2. \quad (\text{A3})$$

When $c = 0$ Eq. (A1) becomes

$$(1 + \alpha^2)\lambda^4 + 2M\lambda^2 + Q = 0, \quad (\text{A4})$$

with the solutions

$$\lambda^2 = \frac{-M \pm \sqrt{M^2 - (1 + \alpha^2)Q}}{1 + \alpha^2}. \quad (\text{A5})$$

In order that the unperturbed eigenvalues are all imaginary, the coefficients must satisfy

$$Q > 0, \quad M > 0, \quad S^2 \equiv M^2 - (1 + \alpha^2)Q > 0 \quad (S > 0), \quad (\text{A6})$$

in which case Eq. (A5) has two negative roots

$$\lambda^2 = -k_{\pm}^2 \equiv \frac{-M \pm S}{1 + \alpha^2}. \quad (\text{A7})$$

For $|c| \ll 1$, the solutions to Eq. (A1) can be written as

$$\lambda = ik_{\pm} + c(\delta_{\pm}^r + i\delta_{\pm}^i) + O(c^2) \quad \text{and} \quad c.c. \quad (\text{A8})$$

At $O(c^1)$, we obtain the following condition:

$$\begin{aligned} 2(i k_{\pm})^2 (1 + \alpha^2) (\delta_{\pm}^r + i \delta_{\pm}^i) + (ik_{\pm})^2 + 2M(\delta_{\pm}^r + i \delta_{\pm}^i) + N \\ = 0, \end{aligned} \quad (\text{A9})$$

which leads to

$$\delta_{\pm}^r = \frac{k_{\pm}^2 - N}{2(M - k_{\pm}^2(1 + \alpha^2))}, \quad \delta_{\pm}^i = 0. \quad (\text{A10})$$

Thus $\delta_{\pm}^r \neq 0$ whenever $k_{\pm}^2 \neq N$ implying that the eigenvalues move off the imaginary axis for $c \neq 0$. Thus, $c = 0$ is a (multiple) bifurcation point.

These eigenvalues move in opposite directions whenever

$$\begin{aligned} \delta_+^r \delta_-^r &= -\frac{(M - (1 + \alpha^2)N)^2 - S^2}{4S^2(1 + \alpha^2)^2} \\ &= -\frac{1}{4S^2(1 + \alpha^2)} \left((1 + \alpha^2)N^2 + Q - 2MN \right) < 0. \end{aligned} \quad (\text{A11})$$

In the last factor, $Q > 0$ and $M > 0$ as required by Eq. (A6), while the sign of N determines the Hopf stability of A_0 in Eq. (2.1).²³ In the case under consideration $\mu < 0$ and the A_0 are Hopf-stable. Thus, $N < 0$ and the eigenvalues do indeed move in opposite directions.

APPENDIX B: TRAVELING FRONTS IN VARIATIONAL PDEs

In this appendix, we consider a variational PDE $u_t = -\delta\mathcal{F}/\delta u$ where $\delta/\delta u$ denotes a functional derivative with respect to u . For such a PDE, if a front separates a left pattern

P_- with free energy density \mathcal{L}_- and a right pattern P_+ with free energy density \mathcal{L}_+ , the front should move with speed $c > 0$ (to the right) if $\mathcal{L}_- < \mathcal{L}_+$, and vice versa. The value of the control parameter r such that $\mathcal{L}_- = \mathcal{L}_+$ is known as the Maxwell point $r = r_M$. We define $\delta r \equiv r - r_M$ as the deviation from the Maxwell point.

If the two patterns P_{\pm} are both spatially homogeneous equilibria, denoted by u_{\pm} , the front then takes the form of a traveling wave $u(x - ct)$ with boundary conditions $u(\pm\infty) = u_{\pm}$. In terms of the free energy densities \mathcal{L}_{\pm} , we have

$$\frac{d\mathcal{F}}{dt} = c(\mathcal{L}_- - \mathcal{L}_+). \quad (\text{B1})$$

On the other hand, using the variational structure we get

$$\frac{d\mathcal{F}}{dt} = \int \frac{\delta\mathcal{F}}{\delta u} u_t dx = - \int u_t^2 dx = -c^2 \int u_x^2 dx. \quad (\text{B2})$$

Equating Eqs. (B1) and (B2), we arrive at the following expression for the front speed:

$$c = (\mathcal{L}_+ - \mathcal{L}_-) / \left(\int u_x^2 dx \right). \quad (\text{B3})$$

Equation (B3), which holds for arbitrary δr , states that the front speed equals the difference in free energy density divided by the L^2 -norm of the Goldstone mode u_x . For $|\delta r| \ll 1$, since $\mathcal{L}_+ - \mathcal{L}_- \sim \delta r$ and $\int u_x^2 dx \sim 1$, the front speed scales as $c \sim \delta r$.

¹Ackemann, T., Firth, W. J., and Oppo, G.-L., “Fundamentals and applications of spatial dissipative solitons in photonic devices,” in *Advances in Atomic, Molecular and Optical Physics*, edited by P. R. Berman, E. Arimondo, and C. C. Lin (Academic Press, 2009), Vol. 57, pp. 323–421.

²Aranson, I. S., Malomed, B. A., Pismen, L. M., and Tsimring, L. S., “Crystallization kinetics and self-induced pinning in cellular patterns,” *Phys. Rev. E* **62**, R5–R8 (2000).

³Barten, W., Lücke, M., and Kamps, M., “Localized traveling-wave convection in binary-fluid mixtures,” *Phys. Rev. Lett.* **66**, 2621–2624 (1991).

⁴Batiste, O., Knobloch, E., Alonso, A., and Mercader, I., “Spatially localized binary-fluid convection,” *J. Fluid Mech.* **560**, 149–158 (2006).

⁵Beck, M., and Wayne, C. E., “Using global invariant manifolds to understand metastability in the Burgers equation with small viscosity,” *SIAM Rev.* **53**, 129–153 (2011).

⁶Bergeon, A., and Knobloch, E., “Spatially localized states in natural doubly diffusive convection,” *Phys. Fluids* **20**, 034102 (2008).

⁷Blanchflower, S., “Magnetohydrodynamic convectons,” *Phys. Lett. A* **261**, 74–81 (1999).

⁸Burke, J., Houghton, S. M., and Knobloch, E., “Swift-Hohenberg equation with broken reflection symmetry,” *Phys. Rev. E* **80**, 036202 (2009).

⁹Burke, J., and Knobloch, E., “Localized states in the generalized Swift-Hohenberg equation,” *Phys. Rev. E* **73**, 056211 (2006).

¹⁰Burke, J., and Knobloch, E., “Homoclinic snaking: Structure and stability,” *Chaos* **17**, 037102 (2007).

¹¹Champneys, A. R., Knobloch, E., Ma, Y.-P., and Wagenknecht, T., “Homoclinic snakes bounded by a saddle-centre periodic orbit,” *SIAM J. Appl. Dyn. Sys.* (submitted).

¹²Coullet, P., Riera, C., and Tresser, C., “Strong resonances of spatially distributed oscillators: A laboratory to study patterns and defects,” *Physica D* **61**, 119–131 (1992).

¹³Coullet, P., Riera, C., and Tresser, C., “Stable static localized structures in one dimension,” *Phys. Rev. Lett.* **84**, 3069–3072 (2000).

¹⁴Cox, S. M., and Matthews, P. C., “Exponential time differencing for stiff systems,” *J. Comput. Phys.* **176**, 430–455 (2002).

¹⁵Dennin, M., Ahlers, G., and Cannell, D. S., “Spatiotemporal chaos in electroconvection,” *Science* **272**(5260), 388–390 (1996).

- ¹⁶Houghton, S. M., and Knobloch, E., "The Swift-Hohenberg equation with broken cubic-quintic nonlinearity," *Phys. Rev. E* **84**, 016204 (2011).
- ¹⁷Hoyle, R., *Pattern Formation* (Cambridge University Press, Cambridge, 2006).
- ¹⁸Kolodner, P., Bensimon, D., and Surko, C. M., "Traveling-wave convection in an annulus," *Phys. Rev. Lett.* **60**, 1723–1726 (1988).
- ¹⁹Krechetnikov, R., and Marsden, J. E., "Dissipation-induced instabilities in finite dimensions," *Rev. Mod. Phys.* **79**, 519–553 (2007).
- ²⁰Lioubashevski, O., Arbell, H., and Fineberg, J., "Dissipative solitary waves in driven surface waves," *Phys. Rev. Lett.* **76**, 3959–3962 (1996).
- ²¹Lombardi, E., "Oscillatory integrals and phenomena beyond all algebraic orders: With applications to homoclinic orbits in reversible systems," in *Lecture Notes in Mathematics* (Springer, 2000).
- ²²Ma, Y.-P., Burke, J., and Knobloch, E., "Defect-mediated snaking: A new growth mechanism for localized structures," *Physica D* **239**, 1867–1883 (2010).
- ²³Ma, Y.-P., and Knobloch, E., "Localized states in the forced complex Ginzburg-Landau equation with 1:1 resonance," preprint (2010).
- ²⁴Pomeau, Y., "Front motion, metastability and subcritical bifurcations in hydrodynamics," *Physica D* **23**, 3–11 (1986).
- ²⁵Rajchenbach, J., Leroux, A., and Clamond, D., "New standing solitary waves in water," *Phys. Rev. Lett.* **107**, 024502 (2011).
- ²⁶Riecke, H., and Granzow, G. D., "Localization of waves without bistability: Worms in nematic electroconvection," *Phys. Rev. Lett.* **81**, 333–336 (1998).
- ²⁷Sandstede, B., "Stability of travelling waves," in *Handbook of Dynamical Systems* (Elsevier Science, 2002), Vol. 2, pp. 983–1055.
- ²⁸Sandstede, B., and Scheel, A., "Defects in oscillatory media: Toward a classification," *SIAM J. Appl. Dyn. Syst.* **3**, 1–68 (2004).
- ²⁹Schneider, T. M., Gibson, J. F., and Burke, J., "Snakes and ladders: Localized solutions of plane Couette flow," *Phys. Rev. Lett.* **104**, 104501 (2010).
- ³⁰Tobias, S. M., Proctor, M. R. E., and Knobloch, E., "Convective and absolute instabilities of fluid flows in finite geometry," *Physica D* **113**, 43–72 (1998).
- ³¹Ueda, K.-I., and Nishiura, Y., "A mathematical mechanism for instabilities in stripe formation on growing domains," *Physica D* **241**, 37–59 (2012).
- ³²Umbanhowar, P. B., Melo, F., and Swinney, H. L., "Localized excitations in a vertically vibrated granular layer," *Nature* **382**, 793–796 (1996).
- ³³van Saarloos, W., "Front propagation into unstable states," *Phys. Rep.* **386**, 29–222 (2003).